EFFECTS OF BETA RADIATION ON NANOSTRUCTURED SEMICONDUCTOR DEVICES FOR LOW ENERGY RADIATION SENSING

A Dissertation

presented to

the Faculty of the Graduate School

at the University of Missouri-Columbia

In Partial Fulfillment

of the Requirements for the Degree

Doctor of Philosophy

---

by

ERIC M. ACOSTA

Prof. Jae W. Kwon, Dissertation Supervisor

December 2021

The undersigned, appointed by the dean of the Graduate School, have examined the dissertation entitled

EFFECTS OF RADIATION ON NANOSTRUCTURED SEMICONDUCTOR DEVICES FOR LOW ENERGY RADIATION SENSING

presented by Eric M. Acosta, a candidate for the degree of Doctor of Philosophy, and hereby certify that, in their opinion, it is worthy of acceptance.

_____

Professor Jae W. Kwon

_____

Professor Scott Kovaleski

_____

Professor Naz Islam

_____

Professor Ping Yu

DEDICATIONS

This dissertation is dedicated to my family, especially my parents, without whom I never would have made it this far. The importance of education is something I learned from my parents, and I now understand very well my dad's saying: "Education makes you free". I hope to use the knowledge and experience I have gained through my doctoral studies to make my family proud and help make the world a better place.

I would also like to thank my friends and colleagues Dilip Venugopal, Ryan McCay, Quang Nguyen, Nanda Kasani, and Michael Buikus. Thank you for all the good times and great conversations.

ACKNOWLEDGEMENTS

I would like to thank my advisor and mentor, Prof. Jae W. Kwon, for the opportunity and support to do research in what I find most interesting. It was quite lucky to meet someone who is as fascinated by energy and its potential as I am.

TABLE OF CONTENTS

ACKNOWLEDGEMENTS ii

LIST OF FIGURES v

ABSTRACT x

Chapter I: Introduction 1

Chapter II: Theory and Design 5

Conditions for Surface Plasmon Resonance 5

Production of Plasmonic Hot Electrons and Charge Multiplication 10

Oxidation Kinetics of Titanium 12

Chapter III: Methodology 18

Fabrication and Study of Nanostructured Titanium Dioxide 18

Fabrication and Testing of TiO_2 nanoparticle samples 31

Chapter IV: Results and Discussion 33

Simulation of Beta Irradiation on TiO_2 33

Effects of Beta Radiation on Barrier Height in Nanoporous Pt/TiO_2 Schottky Diodes 45

Device Improvements by Two-step anodization and Rapid Thermal Annealing . 51

Chapter V: Conclusion 60

Summary 60

Implications and Future Work 61

References 62

VITA 70

LIST OF FIGURES

Figure 1. Graph of the dielectric coefficients as a function of wavelength for some common plasmonic metals. 8

Figure 2. Representation of normal and umklapp phonon-phonon scattering modes 10

Figure 3. Energy band diagrams for hot CM through (a) impact ionization and (b) inverse Auger process in a metal/TiO_2 Schottky diode. The filled dots refer to primary excited (black) and secondary (red) electrons. The empty dots refer to holes. 12

Figure 4. Schematic of the metal oxide energy band diagram of various metal oxide classes with examples of materials belonging to the class. The d-band occupancy determines the conductivity properties of the metal oxide 13

Figure 5. Schematic of the dissolution reactions leading to the formation of pores in TiO_2. The arrows in the pore on the right represent the dissolution rate profile within the pore. 16

Figure 6. SEM images of porous TiO_2. (Left) SEM image of surface prior to Pt coating, (right) SEM image of surface after sputtered Pt coating. 19

Figure 7. Cross-sectional view of the Pt/TiO2/Ti structure 20

Figure 8. EDS analysis of the cross-sectional area of the working electrode. Pt was deposited via sputtering technique. 21

Figure 9. Photo of the ALD sample platter after deposition. The dark area in the center is only lightly coated, and (bottom) the glass and TiO2 samples after platinum coating by ALD. 23

Figure 10. Surface of the TiO_2 samples coated by 400 cycles (left) and 800 cycles (right) of platinum ALD. 24

Figure 11. EDS map of the ALD Pt-coated TiO_2 structure. 25

Figure 12. Top-down view of ALD reactor chamber during continuous mode operation 26

Figure 13. Overview of the ALD exposure mode 27

Figure 14. Cross-sectional image of the porous TiO2 with ALD Pt under exposure mode taken with a backscattered electron detector. The oxide film thickness was measured to be ~1.5 μm and the Pt film was measured to be ~30-40 nm along the surface. 28

Figure 15. EDS color map of the ALD Pt-coated TiO2 porous structures under exposure mode 29

Figure 16. XRD spectrum of the thermally oxidized TiO_2 sample (a) at 450°C in 2 hours, (b) at 500°C in 2 hours, and (c) at 550°C in 2 hours. 30

Figure 17. Schematic structure of the TiO_2 nanoparticles/Pt electrode. 31

Figure 18. XRD spectrum of the TiO_2 nanoparticles on Ti substrate (a) before annealing, and (b) after annealing at 550°C for 5 hours in the air environment. 32

Figure 19. COMSOL simulation results of a TE-mode electromagnetic wave incident on a Pt/TiO_2 film. (a) Porous Pt film geometry, and (b) smooth Pt film geometry. The wavelength was set to 258 nm in both cases. The pore diameter, the distance between pores, and pore depth are 250 nm, 100 nm, and 1500 nm, respectively. The thickness of the Pt film is 25 nm in both cases. The angle of incidence is 0 degrees. 33

Figure 20. COMSOL simulation results of a TE-mode electromagnetic wave incident on a Pt/ TiO_2 nanopore at a wavelength of (a) 100 nm, (b) 200 nm, (c) 300 nm, and (d) 400 nm. The pore diameter, the distance between pores, and pore depth are 250 nm, 100 nm, and 1500 nm, respectively. The thickness of the Pt film is 25 nm. The angle of incidence is 0 degrees. 35

Figure 21. COMSOL simulation results of a TE-mode electromagnetic wave incident on a Pt/ TiO2 nanopore with pore diameters of (a) 125 nm, (b) 250 nm, and (c) 500 nm. The wavelength was set to 258 nm. The pore diameter, the distance between pores, and pore depth are 250 nm, 100 nm, and 1500 nm, respectively. The thickness of the Pt film is 25 nm. 36

Figure 22. Wavelength (energy) dependent dielectric constants of air, Pt, and TiO_2 materials derived from experimentally measured values..... 37

Figure 23. COMSOL model of SPR in nanoporous Pt/TiO_2 devices with pore diameters of (left) 100 nm, and (right) 150 nm. The pore depth is 1500 nm, the thickness of Pt is 25 nm, and the wavelength was set to 66 nm (resonant condition). 38

Figure 24. COMSOL model of SPR in nanoporous Pt/TiO_2 devices with pore a diameter of 150 nm. The pore depth is 1500 nm, the thickness of Pt is 25 nm, and the wavelength was set to 66 nm (resonant condition). The origin boundary of the electromagnetic wave was placed 15 nm above the surface of the pore. 39

Figure 25. CASINO simulation of 17 keV electrons on a Pt/TiO_2/Ti surface showing (a) electron trajectories, (b) energy deposition profile, (c) range distribution of electrons, (d) distribution of backscattered electrons energies, and (e) distribution of angles of backscattered electrons. The simulation consisted of 10,000 electrons as a Gaussian beam having a radius of 10 nm. The film thicknesses were 25 nm, 1,500 nm, and 32,000 nm for Pt, TiO_2, and Ti, respectively. 43

Figure 26. CASINO simulation of 17 keV electrons on a Pt/TiO_2/Ti surface showing (a) average electron range, (b) radial scattering, and (c) backscatter coefficient at various Pt film thicknesses. The simulation consisted of 10,000 electrons as a Gaussian beam having a radius of 10 nm. The film thicknesses were 25 nm, 1,500 nm, and 32,000 nm for Pt, TiO_2, and Ti, respectively. 45

Figure 27. I-V measurements of Pt/TiO_2/Ti Schottky diodes with corresponding semi-log plots. Sample conditions are summarized in Table 1. All measurements were performed in an atmosphere controlled glovebox using a Keithley 2601A Sourcemeter. 47

Figure 28. Schematic diagram of RTA system 53

Figure 29. I-V characteristics of samples fabricated using two-step anodization and treated through RTA. (a, b) RTA sample 1 with corresponding semilog scale plot, and (c,

d) RTA sample 2 with corresponding semilog scale plot. Measurements were taken using a Keithley 2601A sourcemeter under dark conditions. 55

Figure 30. XRD spectra of RTA treated TiO_2 samples. The RTA treatment time was 10 minutes at the specified temperature in a 25 mTorr N_2 environment. 56

Figure 31. I-V measurements of RTA treated TiO_2 Schottky diodes before and during ^{63}Ni beta radiation exposure. (a) I-V characteristics and (b) corresponding semilog scale plot. Measurements were performed in a controlled environment glove box. Measurements were taken using a Keithley 2601A sourcemeter. RTA sample 1 was damaged while loading into the glove box and could not be measured.The total activity of each of the ^{63}Ni foils was 15 mCi and the total activity of the ^{63}Ni deposited on acrylic was 20 mCi. 57

Figure 32. Effect of beta radiation on Schottky barrier height for nanoporous Pt/TiO_2 devices. All devices with nanostructures present exhibit a decrease of the barrier height when exposed to radiation while devices with nanostructures absent exhibit an increase of the barrier height. 59

ABSTRACT

Beta radiation detection currently relies primarily on scintillation detectors. However, the construction of these detectors tends to be large which significantly limits their applicability for field-use. A nanostructured $Pt/TiO_2/Ti$ Schottky device was constructed for use as a compact, low energy radiation detector by making use of surface plasmon resonance which has been shown to enhance energy coupling in similar technologies. The fabrication of the device was done by first electrochemically anodizing a titanium substrate to create a nanoporous surface, followed by annealing to produce a crystalline, semiconducting TiO_2 layer and finally the deposition of the Pt Schottky metal through atomic layer deposition. Modeling of the device using COMSOL software showed the formation of strong electric fields when nanostructures were present. Exposure of the device to low energy ^{63}Ni beta radiation showed a 2-to-3-fold increase to the forward current during radiation exposure without any additional signal amplification. This increase in the current is a consequence of a 2 to 4% lowering of the Schottky barrier height during radiation exposure as well as the production of hot and secondary electrons in the semiconductor. Subsequent improvements to the device using rapid thermal annealing resulted in a nearly 6% decrease of the Schottky barrier height during radiation exposure and a consequent 5-fold increase to the forward bias current in the presence of radiation. Thus, in its current construction the device is capable of being used as a qualitative low energy beta radiation detector.

Chapter I: Introduction

Beta radiation occurs through two emission pathways: 1) β^- decay, in which a neutron is converted to a proton followed by the ejection of a high energy electron and an antineutrino, converting the parent atom to a daughter with a higher proton number but the same atomic number, and 2) β^+ decay, in which a proton is converted to a neutron followed by the ejection of a positron and a neutrino, converting the parent atom to a daughter with a lower proton number but the same atomic number.

Sensing beta radiation is somewhat complex due to the nature of its interactions with matter. Since beta particles have an equal mass to that of orbital electrons, a significant portion of the beta particle energy can be lost in a single encounter, and electron-nuclear interactions can result in abrupt changes to their direction, resulting in a zig-zag travel path. As charged particles, beta particles lose their energy through Coulomb interactions (excitation and ionization) as well as through radiative processes (bremsstrahlung or braking radiation). The three main types of detectors used for beta radiation sensing are 1) gaseous ionization detectors, 2) scintillation detectors, and 3) semiconductor detectors[1]. There are a few subclasses of gas ionization detectors (ion chambers, proportional counters, and Geiger-Mueller tubes) but their principle of operation all rely on producing an electronic output signal originating from the ion pairs formed from the interaction of radiation with the gas within the detector. Scintillation detectors operate on the basis of the conversion of the charged particle kinetic energy into a detectable light signal. Semiconductor detectors rely on the generation and collection of electron-hole pairs (EHPs) produced from incident radiation for detection.

Currently, scintillation counters are the most common technology used for the detection of low-energy beta radiation. However, their major drawback is that the beta-emitting material needs to be physically immersed in the scintillation cocktail to produce a detectable light signal. This, along with the fact that the construction of a scintillation counter often requires the use of bulky electronics, severely limits their applicability for field use. In this sense, semiconductor detectors have an advantage for field applications as they can be made quite compact, but current technology is generally reserved for high energy beta radiation detection as weak beta radiation would not be able to deposit its energy in the active region of the detector. As our knowledge of semiconductors has improved, new materials and fabrication methods have been developed to create semiconductor materials that can outperform silicon in specific niches[2–17].

Recent research has shown that is possible to improve the energy absorption of beta radiation in semiconductors by making use of the principle of Surface Plasmon Resonance (SPR)[18–26]. The term "surface plasmon" was first used by Ritchie in 1957 during his investigations of fast electrons passing through metal films. Since then, there have been considerable advances in the so-called field of plasmonics over a wide spectrum of studies, ranging from electrochemistry to material science and surface-plasmon resonance technology[26]. Surface plasmons are briefly defined as the collective oscillations of conduction electrons at a conductor/non-conductor interface. These oscillations occur due to interactions of an external electric field (that is the result of some form of radiation) with the conductor surface and lead to a change in the electron density on either side of the conductor. The electron density displacement then gives rise to a series of charge density oscillations caused by the coulombic restoring force and creates an electric field inside and

outside of the conductor that is opposite to the external electric field. The phenomenon of charge density oscillations and electric field formation is what is known as surface plasmon resonance or Localized Surface Plasmon Resonance (LSPR)[21].

The SPR technology is an emerging field that has arisen with recent advances in the study of the electromagnetic properties of nanostructured materials. Nanoparticles and nanostructured materials exhibit unique material properties that differ from those of the material in bulk. These material properties are due, in part, to the high surface area to volume ratio of nanostructures and particles. Size-dependent properties also exist, with these becoming more significant when the size of the nanoparticle or nanostructure approaches the de Broglie wavelength of electrons or photons. A few examples of these material properties are self-assembling behavior at fluid interfaces, enhanced optical properties due to surface plasmon resonance of metallic nanoparticles or nanostructures, and superparamagnetism in magnetic nanoparticles[27].

The main focus of SPR has been in the area of photonics as the collective excitations have the ability to concentrate light in subwavelength structures. However, little attention has been given to the interaction of other forms of radiation, such as beta radiation, with surface plasmons. Beta particles have an associated wavelength and frequency, in accordance with the wave-particle duality, and therefore can be treated as an electromagnetic wave that can couple with surface plasmons. This can potentially allow for the enhancement of beta energy absorption[20]. In this work, evidence is found for the excitation of surface plasmons by weak beta radiation in a nanostructured $Pt/TiO_2/Ti$ Schottky diode. The beta radiation-induced SPR phenomena show a clear alteration of the

electrical characteristics of the diode during radioisotope exposure tests. This allows for the potential fabrication of a highly compact device with low-energy beta radiation sensing capabilities.

The next chapter will provide the background, theory of operation and working principles of the nanoporous Pt/TiO_2 Schottky device. Chapter 3 will discuss the experimental methods performed to fabricate the Schottky devices followed by the presentation of experimental measurements of the Schottky devices when exposed to radiation in Chapter 4. Finally, a summary of the research performed as well as implications of research and future work are discussed in Chapter 5.

Chapter II: Theory and Design

Conditions for Surface Plasmon Resonance

Recent research has shown that surface plasmon polaritons can be excited by fast electrons[28–32]. Surface plasmon excitation from electrons can occur by electrons moving both perpendicular as well as parallel to a metal surface. For the case of perpendicular excitation, the wave vector of the surface plasmons is induced by the momentum of electrons in the metal transferred from the incident perpendicular electron beam and the dispersion equation for the surface plasmons only depends on the dielectric functions of the materials with no regard to the beam energy. On the other hand, the surface plasmon wave vector in parallel excitation is determined by the parallel components of the wave vector of the evanescent waves generated by the parallel electron beam, and the operating frequencies of the surface plasmons are determined by working points (the intersection point of the dispersion curve and the beam line). Thus, the operating frequencies through parallel excitation depend both on the dispersion curve as well as the beam energy. Perpendicularly excited surface plasmons contain frequency components, attenuate as they propagate, and are always accompanied by transition radiation, whereas parallelly excited surface plasmons are coherent, tunable, do not attenuate as they propagate, and are not accompanied by transition radiation. Considering the isotropic emission of beta radiation as well as the emission of beta particles through a large energy spectrum, it is possible that beta radiation can result in both perpendicular and parallel excitation of surface plasmons.

A simplistic description of the surface plasmon condition for a model consisting of two semi-infinite nonmagnetic media with frequency-dependent dielectric functions ϵ_1 and

ϵ_2 separated by a planar interface (located at z = 0) is obtained by solving Maxwell's equations in the absence of external sources, presented in Equations (1)-((4).

$$\boldsymbol{\nabla} \times \boldsymbol{H_i} = \epsilon_i \frac{1}{c} \frac{\partial}{\partial t} \boldsymbol{E_i} \quad \textbf{(1)}$$

$$\boldsymbol{\nabla} \times \boldsymbol{E_i} = -\frac{1}{c} \frac{\partial}{\partial t} \boldsymbol{H_i} \quad \textbf{(2)}$$

$$\boldsymbol{\nabla} \cdot (\epsilon_i \boldsymbol{E_i}) = 0 \quad \textbf{(3)}$$

$$\boldsymbol{\nabla} \cdot \boldsymbol{H_i} = 0 \quad \textbf{(4)}$$

where *E*, *H*, *c*, and *i* are the electric field, magnetic field, speed of light, and the index describing the two media, respectively.

In an ideal surface, a wave can only propagate along with the interface when the electric field component is normal to the surface (i.e. p-polarized electromagnetic modes). Considering the x-axis as the direction of propagation, the electric and magnetic field vectors are given by Equations (5) and ((6).

$$\boldsymbol{E_i} = (E_{ix}, 0, E_{iz}) e^{-\kappa_i |z|} e^{i(q_i x - \omega t)} \quad \textbf{(5)}$$

$$\boldsymbol{H_i} = \big(0, E_{iy}, 0\big) e^{-\kappa_i |z|} e^{i(q_i x - \omega t)} \quad \textbf{(6)}$$

where κ, q, and ω are the extinction coefficient, the magnitude of the wave vector parallel to the surface, and wave frequency, respectively.

By boundary conditions, the parallel components of the electric and magnetic fields must be continuous across the interface. Substituting Equations (5) and ((6) into Maxwell's equations ultimately yields Equations (7) and (8):

$$\frac{\kappa_1}{\epsilon_1} H_{1y} + \frac{\kappa_2}{\epsilon_2} H_{2y} \quad \textbf{(7)}$$

$$H_{1y} - H_{2y} = 0 \quad \textbf{(8)}$$

and a solution exists only if the determinant is zero, expressed by Equation (9), and describes the surface plasmon condition.

$$\frac{\epsilon_1}{\kappa_1} + \frac{\epsilon_2}{\kappa_2} = 0 \quad \textbf{(9)}$$

At the point where the extinction coefficient for both media become equal to each other ($\kappa_1 = \kappa_2 = q$), Equation (9) simplifies to Equation (10), and represents the nonretarded surface plasmon condition (i.e. where the phase velocity ω/q is much smaller than c).

$$\epsilon_1 + \epsilon_2 = 0 \quad \textbf{(10)}$$

The surface plasmon energy can be approximated at the point where the real part of the dielectric coefficients are equal to each other (i.e. $|\epsilon_1'| \approx \epsilon_2'$, assuming that $|\epsilon_1'| > \epsilon_2'$)[33]. The associated surface plasmon wavelengths can be approximated by the crossing points of the dielectric functions of the metal and dielectric media. Figure 1 shows the wavelength-dependent dielectric coefficients for some of the most commonly used plasmonic metals with air as the dielectric material. The dielectric coefficients were calculated with the use of the Brendel-Bormann model[34].

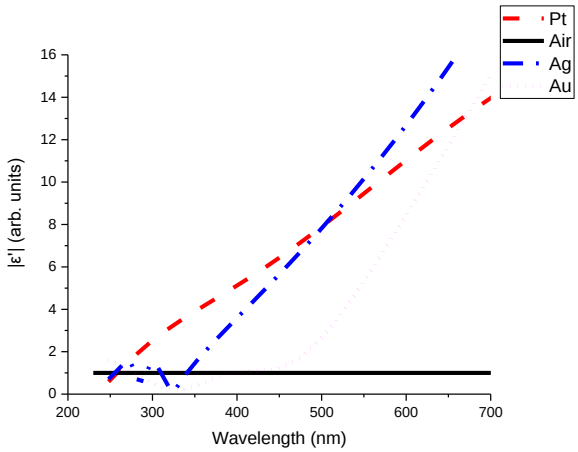

Figure 1. *Graph of the dielectric coefficients as a function of wavelength for some common plasmonic metals.*

Considering an example of a Pt/air interface, the intersection of the dielectric coefficients occurs at a wavelength $\lambda \approx 258$ nm and corresponds to an energy of 4.81 eV. Even weak beta emitters such as ^{3}H produce radiation with a much higher average energy (5.6817 keV) and shorter wavelength. However, beta particles are emitted over a spectrum and betas emitted on the lower end would be capable of exciting surface plasmons. Even high-energy beta particles can couple with surface plasmons by lowering their energy through scattering with the surrounding media.

Surface-plasmon polaritons with phase velocities comparable to the speed of light (i.e. in the retarded region) propagate along the conductor surface with frequencies that range from 0 (at $q = 0$) to the asymptotic Ritchie's frequency $\omega_s = \omega_p/\sqrt{2}$, where ω_p is the plasmon frequency expressed in Equation (11).

$$\omega_p = \sqrt{\frac{4\pi n e^2}{m_e}} \quad \textbf{(11)}$$

where n, e, and m_e are the equilibrium electron density, electron charge, and electron rest mass, respectively. This means that the propagating wave vector is greater than that of incident radiation of the same energy so external radiation would not be capable of exciting surface plasmons on an ideal surface. However, external radiation can couple with surface plasmon-polaritons by introducing surface roughness/gratings or by the mechanism of attenuated total reflection. Surface roughness or gratings on a surface can allow coupling of radiation with surface plasmon-polaritons by providing the necessary momentum via *umklapp* (U) processes[26] (Figure 2).

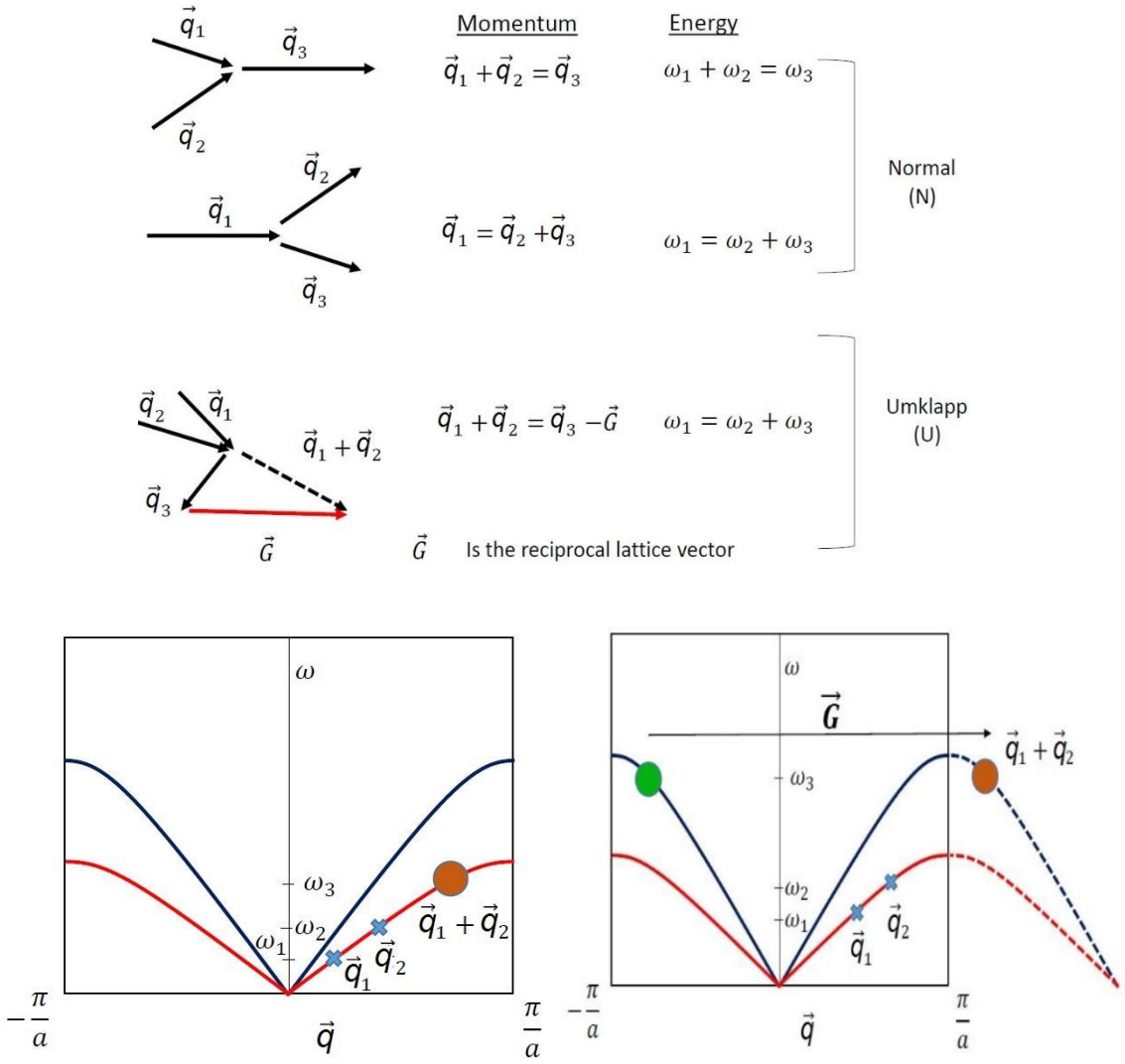

Figure 2. *Representation of normal and umklapp phonon-phonon scattering modes*

Production of Plasmonic Hot Electrons and Charge Multiplication

An analogous technology to solid-state radiation detectors is photo detectors, as they produce signals using the same overall principle of EHP generation through the deposition of energy in a semiconductor junction.

It was initially believed that photo detectors and photovoltaics could only reach a maximum conversion efficiency of about 30% (i.e. the Schokley-Queisser limit)[35], due to

the difference between the incident photon energy and the minimum energy required for EHP generation that would ultimately be dissipated as heat. The advent of quantum dots presented a possibility for increasing the maximum theoretical conversion efficiency as quantum dots could utilize both hot carriers as well as secondary electrons generated from hot carriers before thermalization[36]. Considering this, high energy radiation incident on an absorber can effectively create more than two EHPs before the excess energy is lost as heat (a phenomenon termed "charge multiplication" (CM))[37,38]. After the generation of a hot carrier due to incident radiation, energy relaxation occurs primarily through either phonon scattering (resulting in the carrier energy being dissipated as heat) or through carrier-carrier interactions in which the energy relaxation process results in the production of secondary electrons below the chemical potential. The total number of EHPs generated is a function of the energy of the primary excited electron, as well as the probability of carrier-carrier interaction scattering (also referred to as impact ionization)[37,39]. The total current generated in a metal-semiconductor junction (i.e. a Schottky junction) is the sum of the contributions from impact ionization, the inverse Auger process, and the band-to-band excitation when the energy is absorbed in the semiconductor layer. In the impact ionization process, the primary excited electrons lose their energy through carrier-carrier scattering before thermalization and the generation of phonons. This results in the production of secondary electrons with sufficient energy to overcome the Schottky barrier (Figure 3a). The inverse Auger process consists of excited electrons with energies lower than the Schottky barrier scattering with electrons in the valence band. The electrons gain sufficient energy through the scattering processes to overcome the barrier (Figure 3b). However, impact ionization is the dominant process when the incident radiation is highly energetic[37].

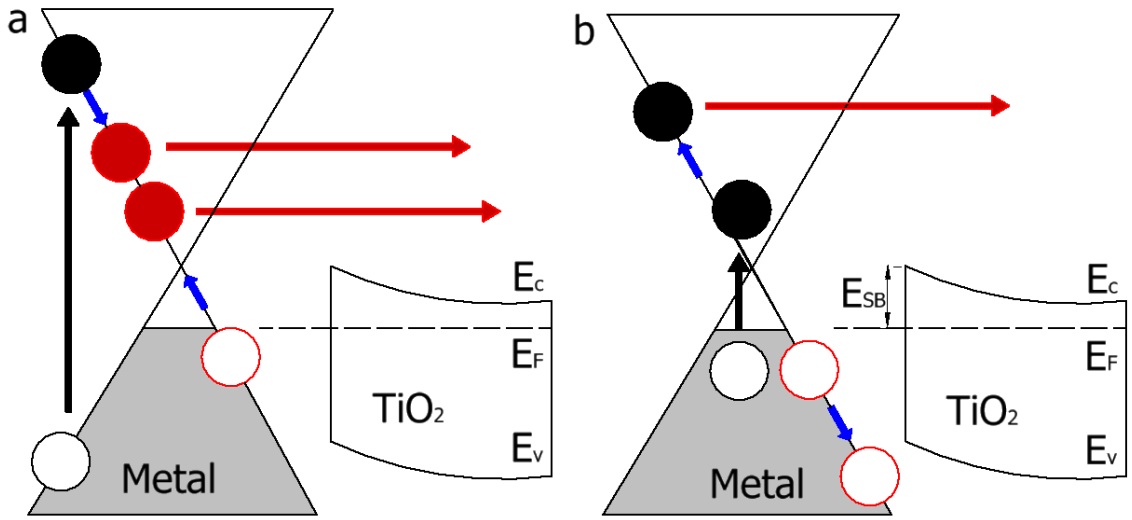

Figure 3. *Energy band diagrams for hot CM through (a) impact ionization and (b) inverse Auger process in a metal/TiO_2 Schottky diode. The filled dots refer to primary excited (black) and secondary (red) electrons. The empty dots refer to holes.*

Oxidation Kinetics of Titanium

Transition metal oxide semiconductors have attracted a lot of attention in recent years, due to their wide range of work functions, high melting temperatures, robustness against chemical attack, and relative ease of fabrication. The material properties of transition metal oxide semiconductors have allowed for their use in a wide array of applications such as energy conversion, energy storage, sensors, diodes, and transistors, among others[10,11].

Transition metal oxides can act as dielectrics, insulators, semiconductors, or conductors depending on their electronic structure. The conductivity properties of oxides arise from a combination of electrostatic, geometrical, and quantum chemical characteristics. In most cases, the qualitative features of the oxide's electronic structure can

be understood with simple models like crystal field theory, ligand field theory, and d-band occupancy. Most metal oxides are arranged in a tetrahedral or octahedral geometry with the oxygen anions surrounding the metal cation. Although the approach to qualitatively describing the electronic structure of the oxide differs between crystal field theory and ligand field theory, they both yield a similar model where there is a splitting of the d-orbital energies and ultimately results in an energy gap[13]. Metal-oxides can be grouped into different classes according to the level of their d-band occupancy; these are presented in Figure 4.

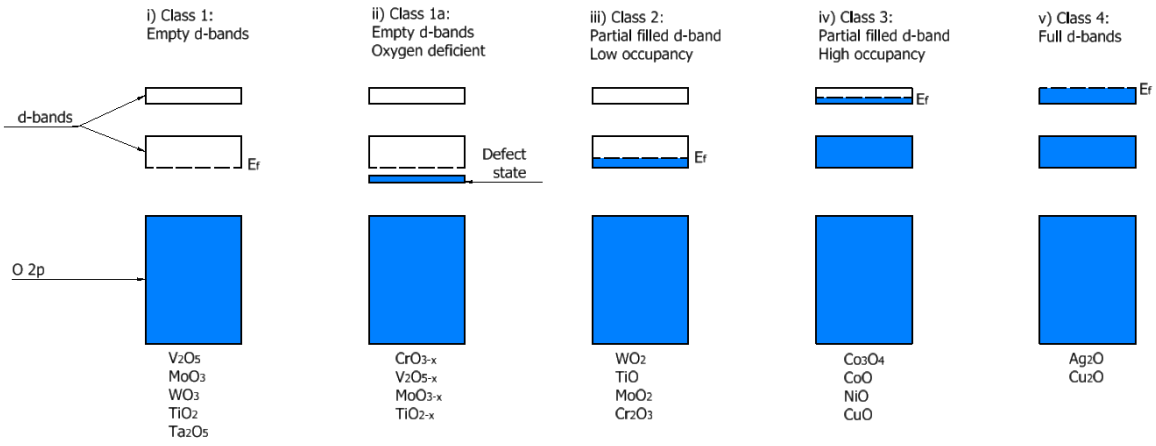

Figure 4. *Schematic of the metal oxide energy band diagram of various metal oxide classes with examples of materials belonging to the class. The d-band occupancy determines the conductivity properties of the metal oxide*

Of the four general metal oxide classes, we are most concerned with oxides belonging to class 1 and class 1a as they generally behave as semiconductors. Class 1 oxides behave as insulators in their completely stoichiometric form, but they have a natural tendency to form oxygen vacancies. This results in the material exhibiting n-type

semiconducting properties. Class 1a oxides also behave as n-type semiconductors due to a high degree of oxygen deficiency.

Titanium dioxide (TiO_2) is a material of particular interest not only due to the material properties described earlier, but its availability also makes it a very cost-effective material[40–49]. As a semiconducting material, TiO_2 has a band gap ranging from ~3.0 eV to 3.2 eV, depending on the dominating crystalline phase[13,43]. The band gap is an important parameter to consider particularly in energy harvesting transistors.

Bare titanium readily oxidizes even under environmental conditions (i.e., atmospheric pressure and room temperature) and forms a thin (~5-10 nm in thickness), amorphous oxide film. However, most cases require a much thicker oxide film and a specific crystalline phase. Oxidation of titanium at high temperatures promotes the growth of the oxide layer as well as the development of a crystalline phase[44,45,50]. The three main crystalline phases of TiO_2 are rutile, anatase, and brookite. The phase that forms depends on the method and parameters used for the oxidation process.

Thermal oxidation of TiO_2 is perhaps the simplest method of developing the oxide since it can be achieved by simply controlling the oxidation temperature and time (though high-quality oxide films also require a controlled pressure environment as well as control over the types of gases present). Studies conducted on the oxidation kinetics have shown that the oxide film grows rapidly during the first 20 minutes, after which a steady-state process is reached. Oxidation temperature is generally a more important parameter for the oxide growth than the treatment time[45,50].

At low temperatures (<400°C) the oxide film growth occurs according to the inverse logarithmic law and is dominated by migration of ionic species in response to the electric field that forms between the metal-oxide and oxide-air interfaces. At high temperatures (>650°C) the oxidation kinetics become dominated by diffusion and the film growth rate becomes parabolic. The oxide film growth at intermediate temperatures occurs by a combination of parabolic and inverse logarithmic law, though the mechanism has not been fully explained at the present time[50].

Various nanostructures can be made from TiO_2 such as pores, tubes, rods, and particles, with the first two types of structures being fabricated via top-down methods while the latter two are most often made by bottom-up approaches.

Electrochemical anodization of Ti is one of the most common methods for fabricating nanopores and nanotubes[44,51–53]. Pores and tubes have very similar surface morphologies, but the mechanism for their formation is different. Nanotube formation can be considered an extension of the pore formation process. TiO_2 nanopores and nanotubes are the product of two competing, electric field-assisted reactions in electrolytes containing fluoride ions. In the initial stage, titanium metal is hydrolyzed to form TiO_2 as described by Equation (12)[54].

$$Ti^{4+} + 2H_2O \rightarrow TiO_2 + 4H^+ \qquad \textbf{(12)}$$

Simultaneously, as the oxide is formed, chemical dissolution of TiO_2 occurs at the oxide/electrolyte interface as shown in Equation (13)[54].

$$TiO_2 + 6HF \rightarrow [TiF_6]^{2-} + 2H_2O + 2H^+ \quad \textbf{(13)}$$

Although the exact nature of the formation of nanopores is still not fully understood, several hypotheses exist. Many researchers believe that nanopores develop from a random local dissolution of TiO_2. As the oxide film thickness is reduced, the electric field becomes more intense near the bottom of the pore, which then promotes new oxide growth. The dissolution of TiO_2 is repeated at the bottom of the pore and results in the pore going deeper into the titanium substrate. Other researchers suggest that the dissolution of TiO_2 does not happen randomly and is actually a consequence of local surface perturbations. This argument explains that fluoride ions migrate to regions of high strain, followed by the migration of hydrogen ions in order to preserve charge neutrality, and induce the dissolution of titanium ions. A schematic representation of the pore formation process is presented in Figure 5.

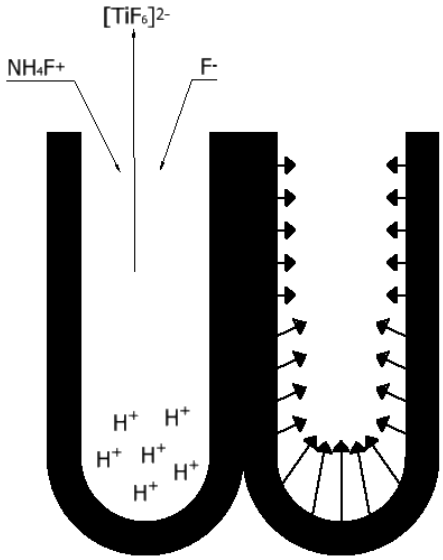

Figure 5. *Schematic of the dissolution reactions leading to the formation of pores in TiO_2. The arrows in the pore on the right represent the dissolution rate profile within the pore.*

Once the pores have successfully formed, they must separate to form separate nanotubes. The nanotube formation process is also the subject of debate among researchers. One theory is that nanotubes are the result of simultaneous development of pores and voids as it is believed that the unanodized regions are prone to field-assisted oxidation and dissolution reactions. A competing idea is that the transition from pores to nanotubes is the result of coulombic interactions between cation vacancies. Cation vacancies arise in the electrolyte from the dissolution of titanium ions and migrate toward the regions between the pores in accordance with the electric field direction. The cation vacancies can then condense in the regions between pores to form voids if the dissolution rate at the metal-oxide interface is higher than the generation of oxygen vacancies required to sustain charge neutrality[54].

TiO_2 nanoparticles and nanorods are commonly synthesized via chemical reduction techniques, such as the hydrothermal method. Briefly, the process consists of dissolving TiO_2 in a base solution and subjecting it to a high temperature for an extended period of time. The nanorod formation process can be considered as an extension of the nanoparticle formation, with nanorods requiring lower temperatures but longer times than nanoparticles [47,55].

Chapter III: Methodology

Fabrication and Study of Nanostructured Titanium Dioxide

Titanium foils of thicknesses 32-μm and 127-μm purchased from Alfa Aesar and Sigma Aldrich were cut and cleaned through a sequence of acetone, methanol, and deionized water. Two pathways were followed for the nanostructured TiO_2 layer of the device: nanopores and nanoparticles. Nanopores were formed by electrochemical anodization of the Ti foils using a solution of ethylene glycol, ammonium fluoride, and deionized water using a Pt counter electrode. Nanoparticles were deposited on the substrate surface through a dip coating method in a solution of TiO_2 nanoparticle powder purchased from Sigma Aldrich mixed in isopropanol. Following the anodization or dip coating procedures, the foils were annealed in a tube furnace at various temperatures to control the crystalline phase of TiO_2. The Pt Schottky contact was deposited using an Atomic Layer Deposition (ALD) reactor varying the number of cycles to control the thickness of the Pt layer.

Electron microscopy was used to assess the structure of the porous TiO_2 film, and its relationship with the titanium substrate and platinum electrode film. A scanning electron microscope (SEM) obtained clear images of the porous surface of the anodized TiO_2. The approximate pore size was measured to be 87.8 nm, which appears to be fairly consistent throughout the sample (Figure 6). The initial sample fabrication process involved the deposition of the Pt Schottky metal through a physical vapor deposition technique (sputtering). However, the SEM image taken after the electrode was coated with sputter-deposited Pt showed the nanopores were completely covered.

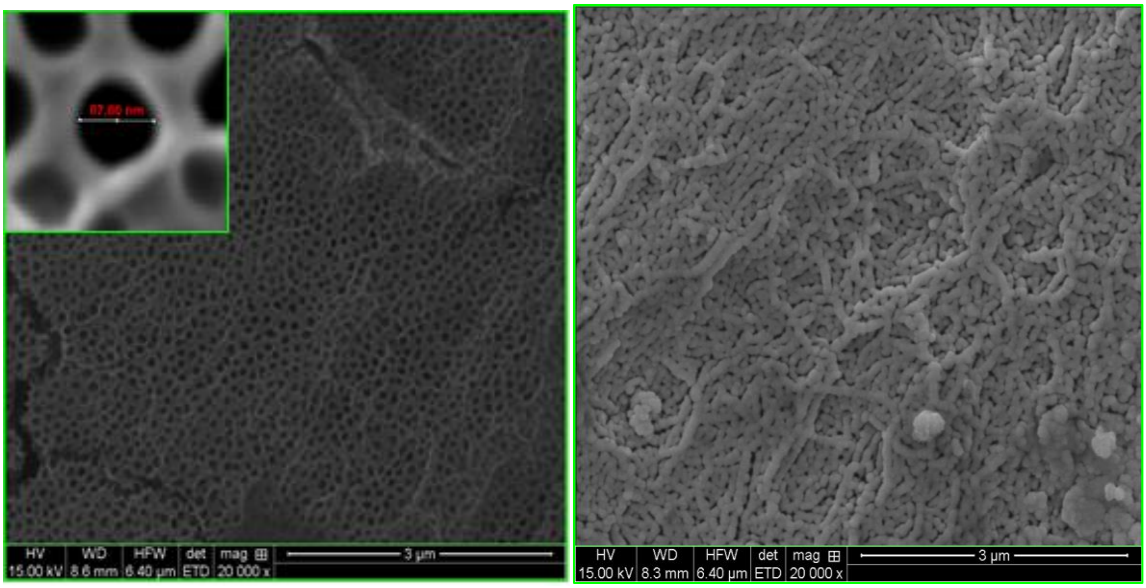

Figure 6. *SEM images of porous TiO_2. (Left) SEM image of surface prior to Pt coating, (right) SEM image of surface after sputtered Pt coating.*

A focused ion beam / scanning electron microscope (FIB-SEM) system obtained cross-sectional images of the materials by milling into the sample and subsequently imaging. The images show a remarkably vertical orientation of the TiO_2 pores, which extend through the entire oxide layer down to the titanium substrate, with an overall film thickness of approximately 7 µm. The interface with the substrate is flush, with no voids or delamination. Although the titanium surface is rough (un-polished and partially etched due to the native oxide removal process), the orientation of the porous TiO_2 is consistently vertical at the interface. Near the surface, the pores become slightly disoriented and a defect site can be seen in a portion of the sample as seen in Figure 7. The platinum film appeared to have minimal penetration into the porous structure. The film was approximately 135 nm thick, which is considerably larger than the pore diameter (~80 nm). Moreover, the

sputtering process tends to be associated with grain sizes in the 20+ nm range, which is too large to achieve deep penetration and coating of such narrow pores.

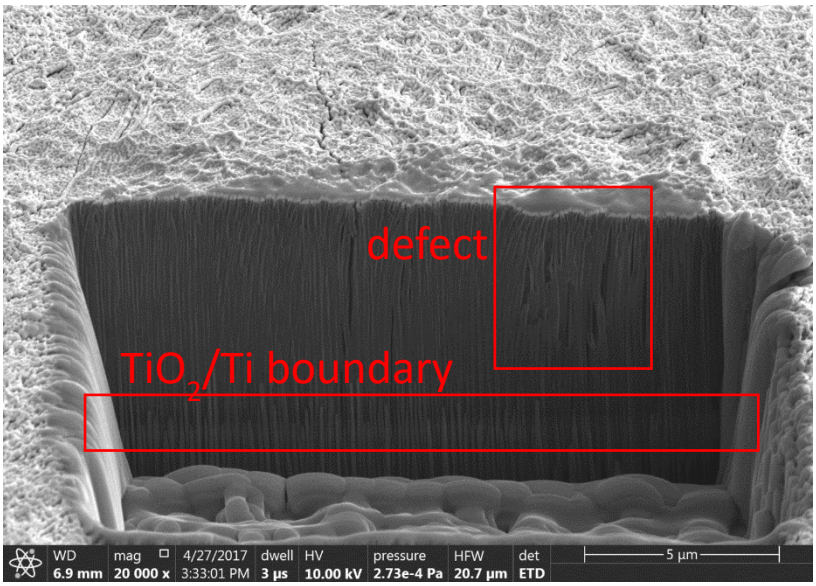

Figure 7. *Cross-sectional view of the Pt/TiO2/Ti structure*

An Energy Dispersive X-ray Spectroscopy (EDS) analysis of the sample shows that the boundary between Ti and TiO_2 is distinctly defined along the vertical axis, with small oxygen content in the titanium, which can likely be attributed to the metallurgy. This tool shows the platinum's boundary with greater precision and clarity, allowing us to see that there is a small platinum content which penetrates into the TiO_2 layer (seen as a blurring of cyan color in Figure 8 near the boundary, although it is not enough to form a continuous film or even grains. Nonetheless, it is clear that the platinum coating within the pores is insufficient.

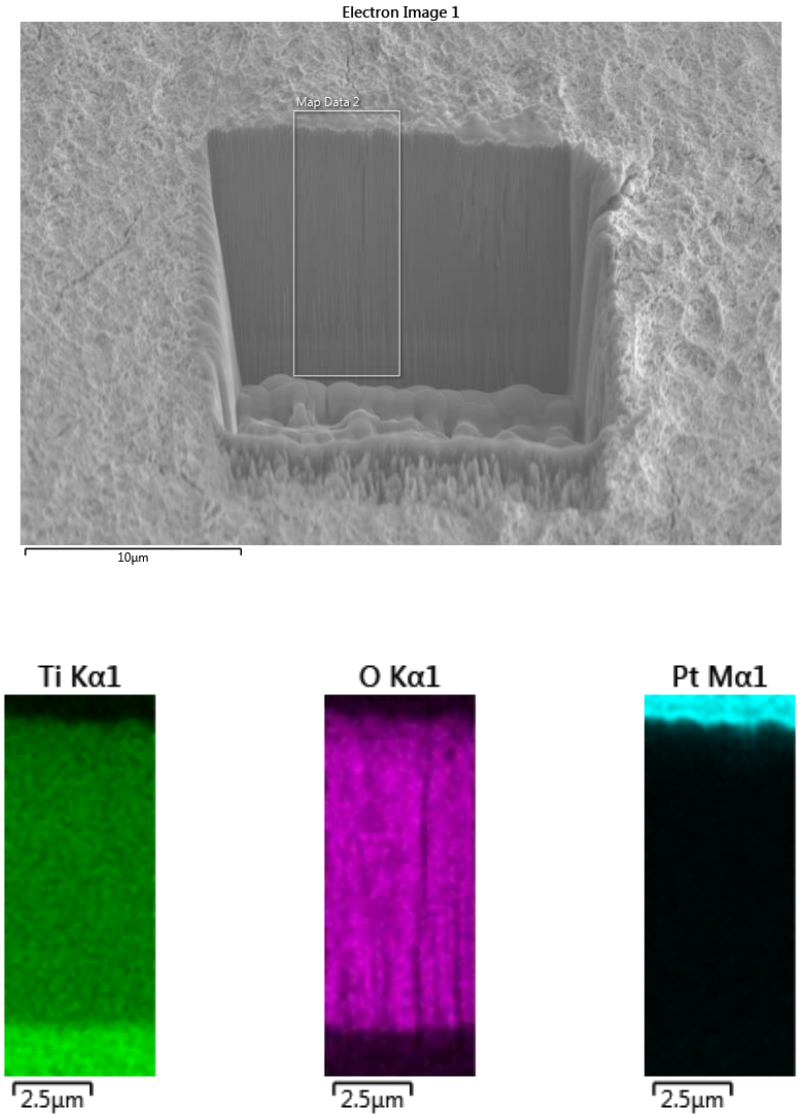

Figure 8. *EDS analysis of the cross-sectional area of the working electrode. Pt was deposited via sputtering technique.*

The ALD process is a much better alternative to achieve a conformal coating in high aspect ratio structures and was thus chosen as the preferred method for depositing the Pt Schottky contact. This process works by alternating pulses of a platinum precursor with oxygen. The platinum atoms are bound to a ligand, which adsorbs on the surface of the substrate upon contact. Oxygen then reacts with the adsorbed monolayer to remove the

organic ligand, leaving only platinum on the surface. The ALD system was modified to include a platinum precursor cylinder and a low flow oxygen gas input, accordingly.

Platinum growth from the ALD process is limited in the initial stages by poor nucleation, which causes a non-linear growth rate until the adsorbed material transitions from island-like nucleation sites to a continuous film. Subsequent cycles produce linear film growth, the rate of which can be controlled to some degree by the sample temperature. The initial TiO_2 samples for platinum coating were located in the center of the sample platter and exhibited film growth on their surfaces (Figure 9). These samples were retained in the system in the same location for the second deposition, while two more were added. A comparison of the Kapton® tape which secured both sets of samples shows that while a single 400-cycle deposition does not appear to grow a platinum film on the Kapton®, the tape which was present through two depositions is coated by a thin film. This indicates that while nucleation is poor and slow on this material, a film can eventually take hold and begin to grow.

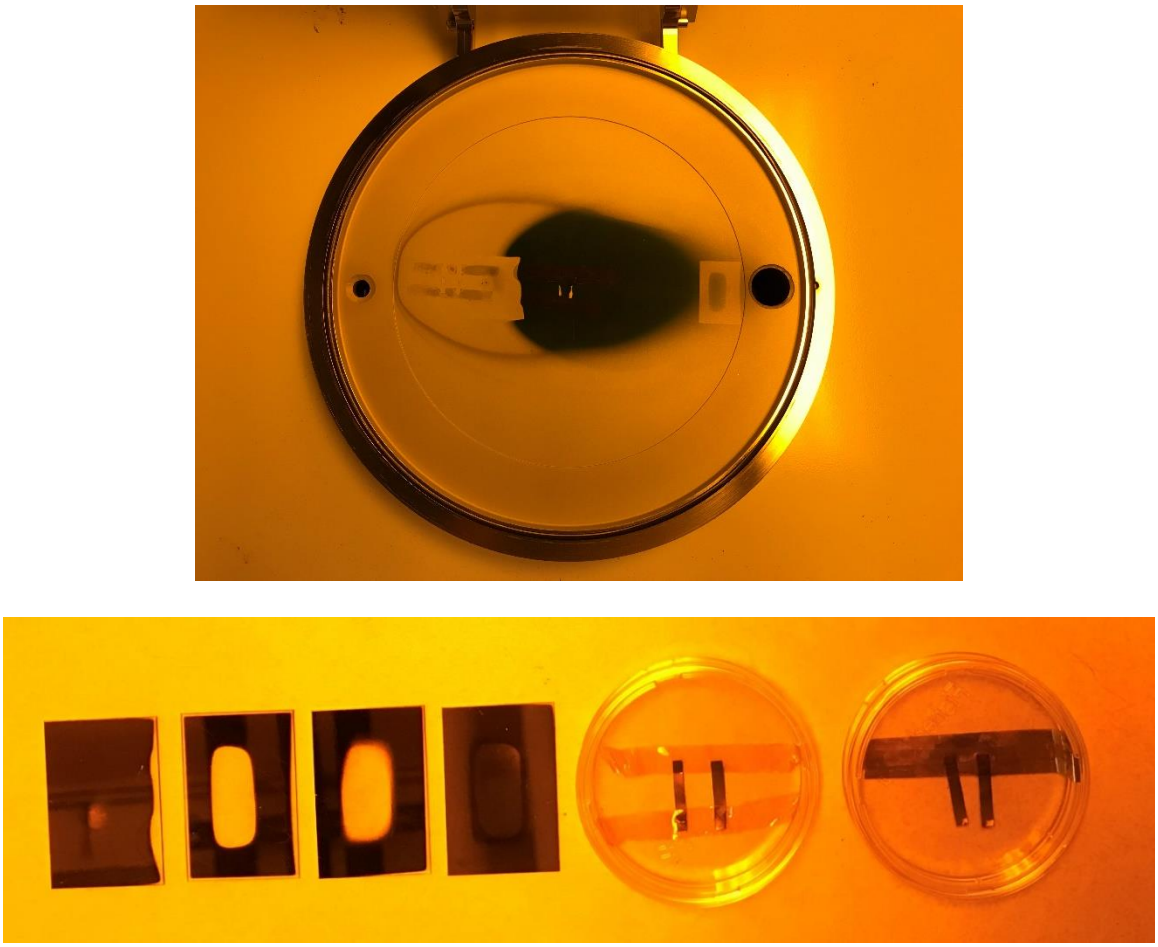

Figure 9. *Photo of the ALD sample platter after deposition. The dark area in the center is only lightly coated, and (bottom) the glass and TiO2 samples after platinum coating by ALD.*

An FIB-SEM was used to analyze the TiO2 sample after Pt-ALD (Figure 10). The sample which was coated with only one 400-cycle process was observed to have a pore diameter after platinum deposition of approximately 80 nm and was most consistent throughout the sample. The thickness of the porous TiO_2 layer was in the 2.5-3 μm range. By contrast, the pore structure on the sample which was coated twice exhibited less uniform pore diameters ranging from 75 to 125 nm, and a TiO_2 thickness of approximately 1.2 μm.

The additional ALD cycles appeared to affect the surface topology of the platinum coating, which in turn affected the porous surface.

An EDS analysis of the samples revealed that the ALD platinum did indeed penetrate into the deep regions of the pores, as desired (Figure 11). Although the SEM image shows horizontally-striated patches of platinum, we believe that this is a result of the FIB milling process. The platinum coating is extremely thin (~25 nm) and is thus easily removed by the focused ion beam (FIB). The EDS is able to detect platinum that may be located in subsequent pores behind the milled area and shows substantial platinum throughout the entirety of the TiO_2 structure. Silicon was also detected and was later found to be from contamination in the annealing furnace.

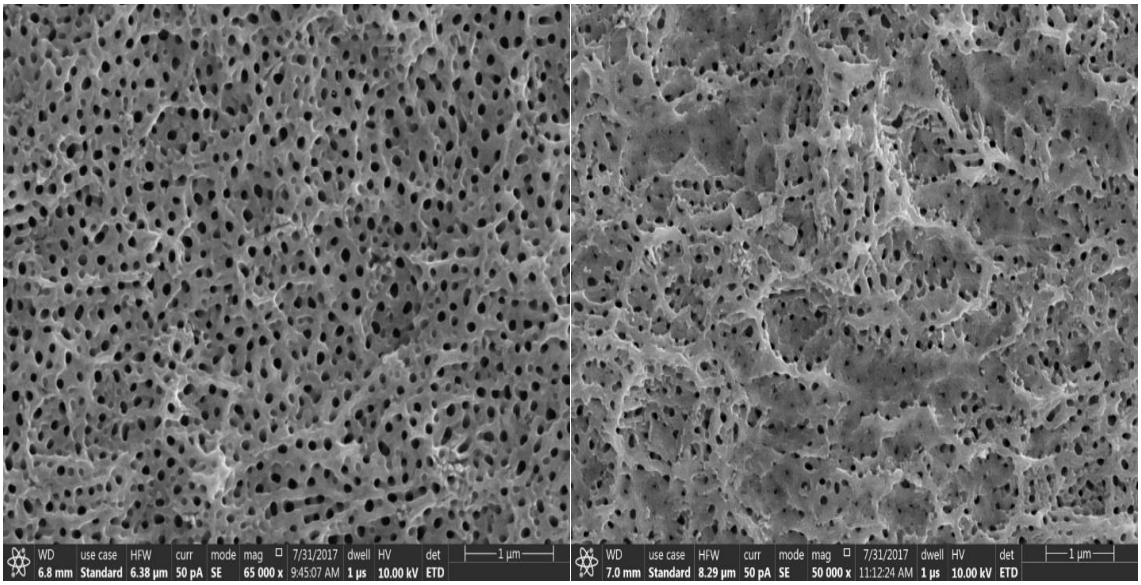

Figure 10. *Surface of the TiO_2 samples coated by 400 cycles (left) and 800 cycles (right) of platinum ALD.*

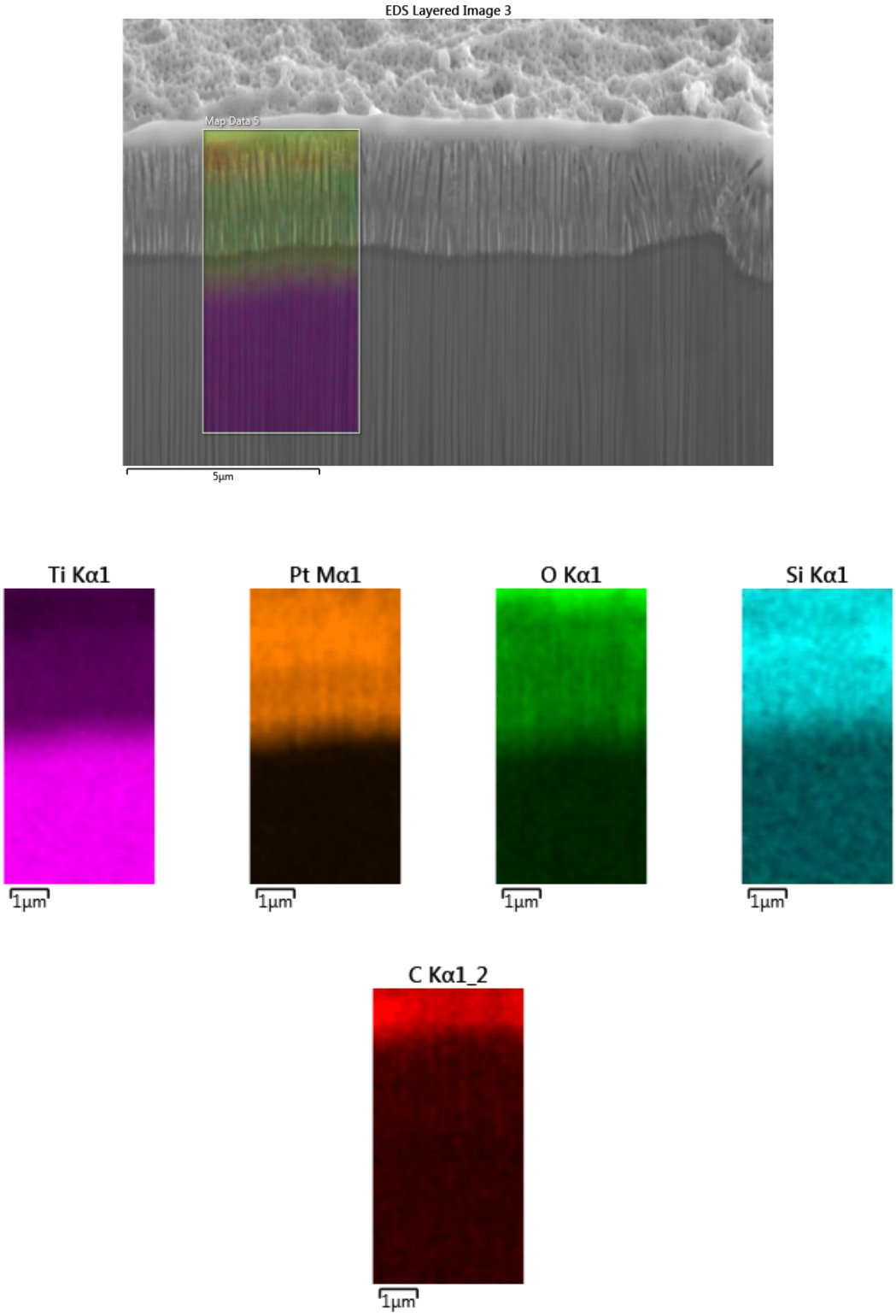

Figure 11. *EDS map of the ALD Pt-coated TiO_2 structure.*

The quality of the platinum film on the nanoporous TiO_2 samples was improved by modifying the recipe on the ALD system. The ALD system is capable of operating in two modes: continuous and exposure mode.

The continuous mode is performed while having the stop valve to the vacuum pump open at all times. Under this setting, the precursor gas and purging gas are flowing continuously from inlet to outlet. This mode is suitable for structures of aspect ratio <40:1. However, the positioning of samples in the reactor is an important factor as the platinum deposition will be greatest along the line of flow of gas from the inlet to outlet ports as shown in Figure 12.

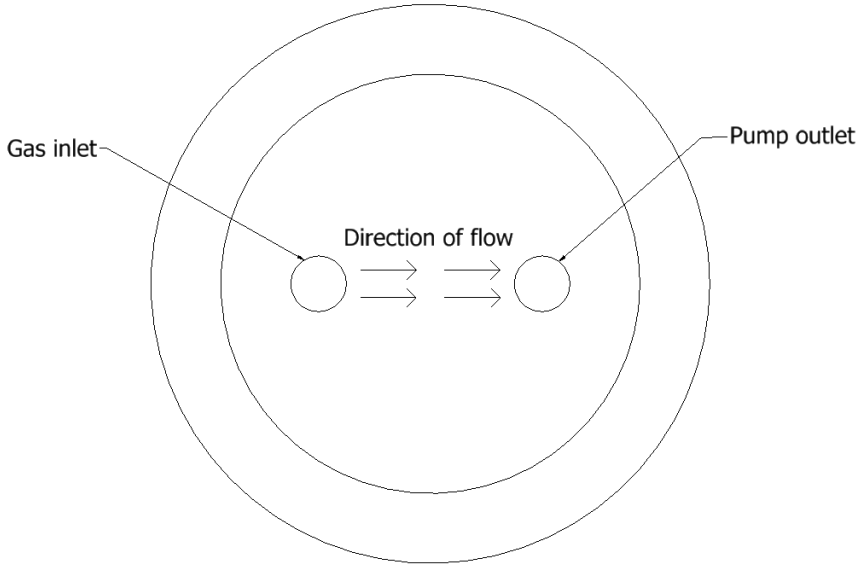

Figure 12. *Top-down view of ALD reactor chamber during continuous mode operation*

The exposure mode operation can be used for coating ultra-high aspect ratio structures. In this mode, the stop valve to the vacuum pump is closed prior to pulsing the precursor and purging gases which isolates the chamber from a dynamic vacuum. The

exposure time depends on the substrate, temperature of deposition, and the material being deposited. By isolating the chamber to static vacuum and allowing the gas to remain in the chamber for some time, gas molecules can diffuse deep into trenches and pores and result in a conformal coating along the entirety of the high aspect ratio structure. An overview of the exposure mode recipe is presented in Figure 13.

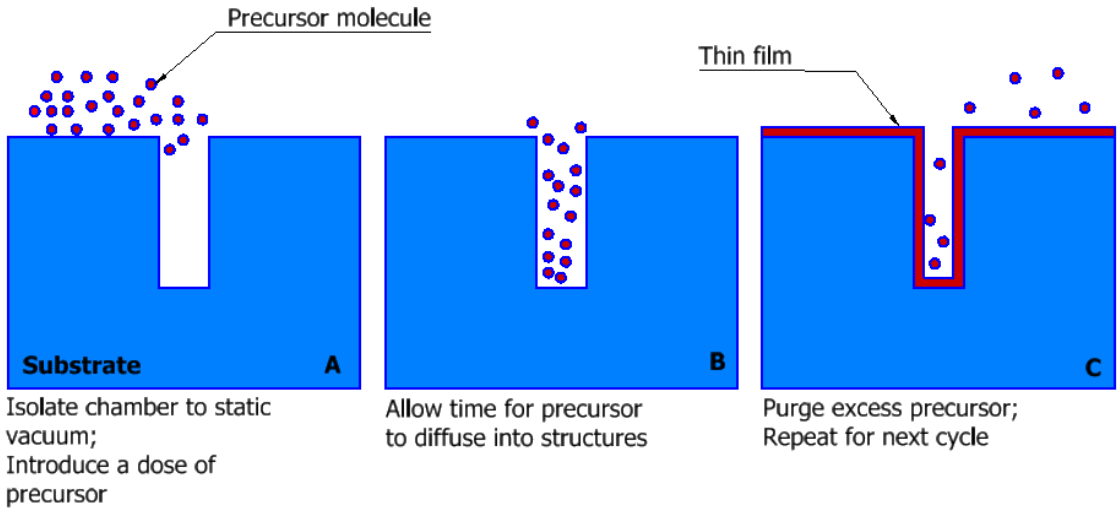

Figure 13. *Overview of the ALD exposure mode*

The exposure mode is not only capable of coating high aspect ratio structures, but it also has the benefit that deposition of material becomes uniform regardless of the position in the reactor chamber. It is also possible to reduce the number of cycles to obtain the same film thickness as in continuous mode which allows for more efficient use of the metal precursor material.

Cross-sectional images of working electrodes fabricated using the exposure mode were taken with an FIB-SEM in order to observe the film within the pores (Figure 14).

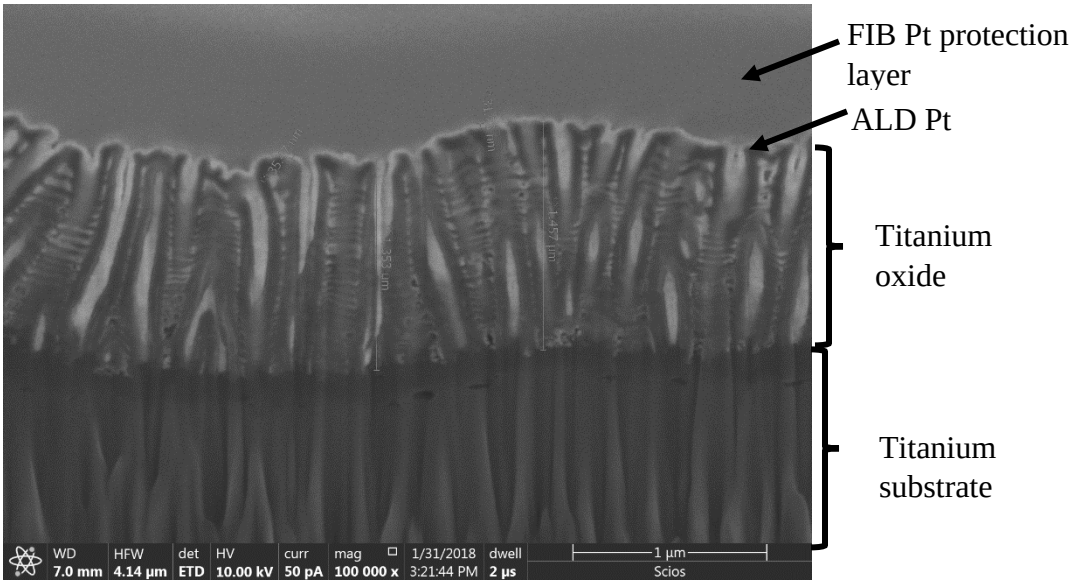

Figure 14. *Cross-sectional image of the porous TiO2 with ALD Pt under exposure mode taken with a backscattered electron detector. The oxide film thickness was measured to be ~1.5 µm and the Pt film was measured to be ~30-40 nm along the surface.*

Backscattered electron images are useful to observe the difference in material composition by the contrast in the image. Four regions can be identified in Figure 14: the titanium substrate, titanium oxide pores, ALD platinum layer, and the FIB platinum protection layer. It can be observed that the ALD platinum film is continuous and coated the walls of the pore structures. To confirm these findings, EDS mapping was conducted on the cross-sectional image of the sample (Figure 15). The EDS map shows that Pt was able to penetrate to the bottom of the pores and is deposited evenly throughout the nanoporous oxide layer. The color map also shows that we were successful in eliminating the source of the silicon contaminant that we had previously observed.

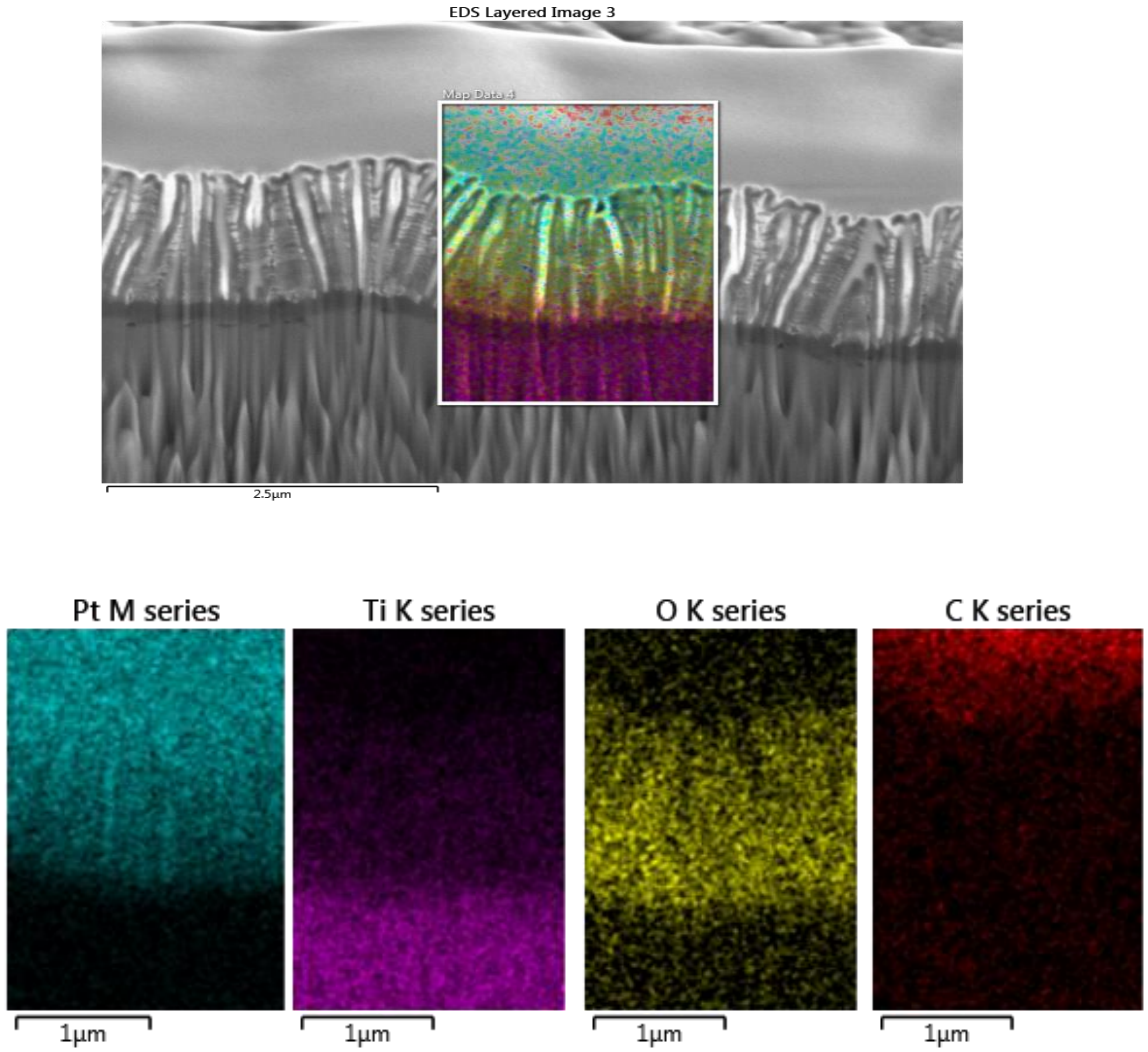

Figure 15. *EDS color map of the ALD Pt-coated TiO2 porous structures under exposure mode*

X-ray Diffraction (XRD) spectroscopy was used to understand more about the crystal structure of TiO_2 nanotubes under various annealing temperatures. Several TiO_2 nanotube samples were fabricated with the same conditions for the study except for the final annealing temperature. For the annealing step, the samples were annealed in air at three different temperatures: 450^{o}C, 500^{o}C, 550^{o}C. The ramping time for all processes was one hour and the annealing time was two hours. The samples were allowed to cool down naturally.

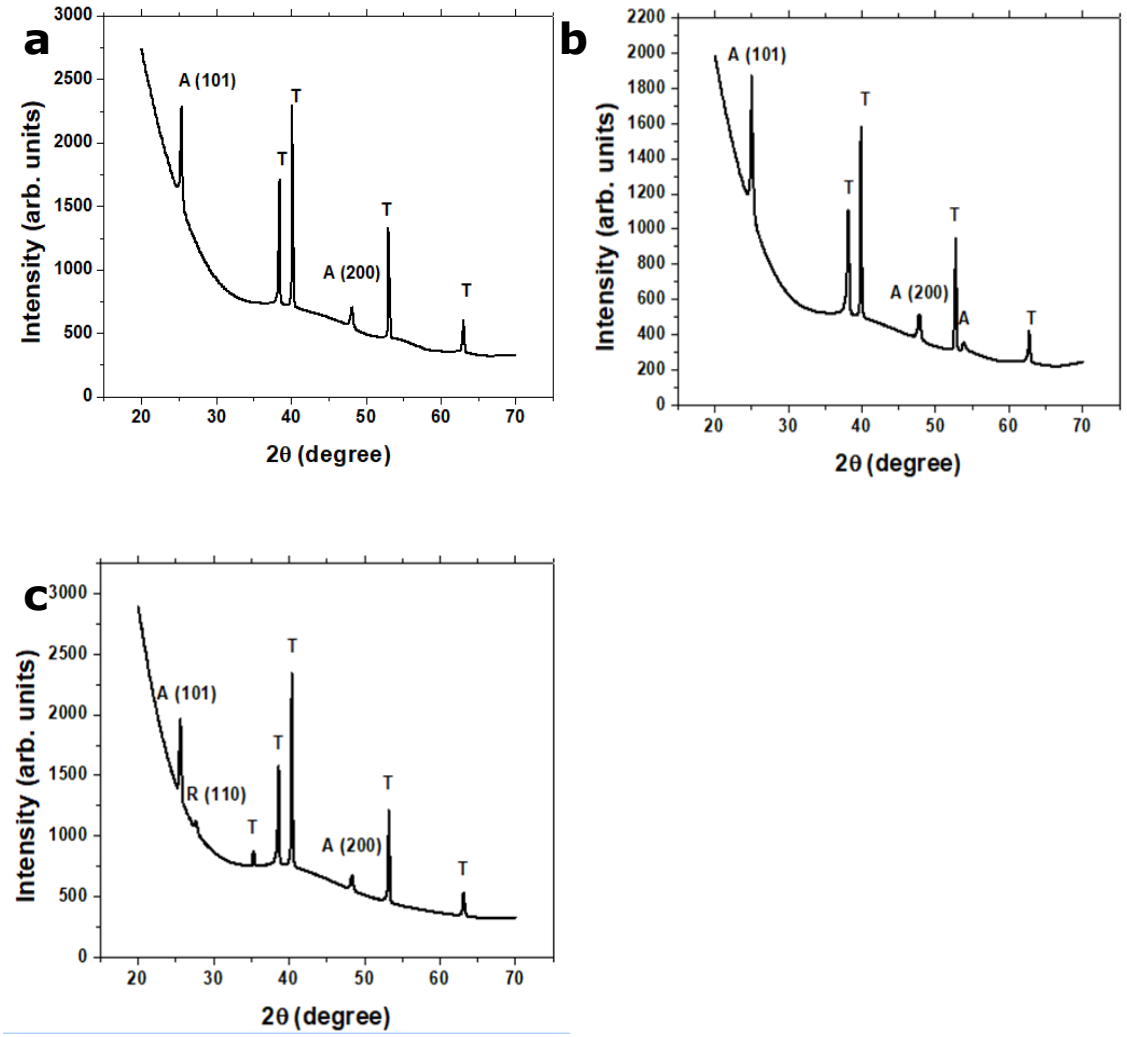

Figure 16. *XRD spectrum of the thermally oxidized TiO_2 sample (a) at 450°C in 2 hours, (b) at 500°C in 2 hours, and (c) at 550°C in 2 hours.*

The results of the samples annealed at different temperatures of 450^{o}C, 500^{o}C, and 550^{o}C are shown in Figure 16a, b, and c, respectively. The 450°C sample only shows an anatase (101) peak and anatase (200) peak. No rutile peak is found on the XRD spectrum of the sample annealed at 450^{o}C. Similarly, the sample annealed at 500^{o}C does not have any rutile peaks. However, it does have an additional anatase peak at 54 degrees. This peak might be too small in the 450^{o}C sample which could be covered by the background signal.

The sample annealed at 550°C has a rutile (110) peak apart from other anatase peaks shown in other samples. Rutile is usually preferred as a dielectric material while anatase is used for its higher electron conductivity. The mixture of rutile and anatase is sometimes used for its enhanced charge separation in photocatalyst applications.

Fabrication and Testing of TiO_2 nanoparticle samples

We studied the properties of Ti samples that were coated with TiO_2 nanoparticles using a dip coating method (Figure 17). The thickness of the TiO_2 nanoparticle film was controlled by adjusting the concentration of the TiO_2 nanoparticle powder in the isopropanol solution. The TiO_2 nanoparticles were then coated with Pt using the ALD process.

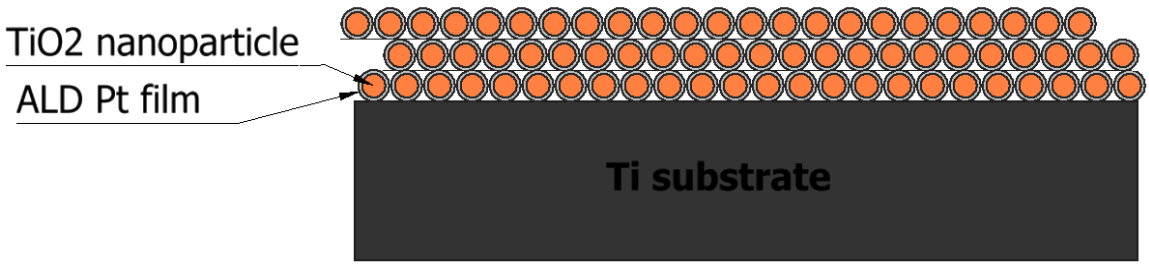

Figure 17. *Schematic structure of the TiO_2 nanoparticles/Pt electrode.*

The XRD pattern of TiO_2 nanoparticles samples before annealing is shown in Figure 18a. The 2θ peak at 25.4° is the anatase (101), confirming that TiO2 nanoparticles have anatase structure before annealing as specified by the manufacturer. The diffraction peaks at 25° and 48° without noticeable rutile peak shows that TiO_2 nanoparticles samples before annealing are mostly comprised of anatase phase. The intensity of XRD peaks also indicates that the nanoparticles are crystalline. The diameter of these nanoparticles is about

25nm. After annealing, the XRD spectrum shows additional rutile (110) and other rutile peaks together with the anatase peaks. The XRD spectrum of the TiO_2 nanoparticles on Ti substrate after annealing is shown in Figure 18b. The spectrum confirms that the nanoparticles are a mixture of anatase and rutile phases after the annealing process. The composition of the TiO_2 phase has a significant impact on the performance of the TiO_2 nanoparticles/Pt electrode as mentioned previously.

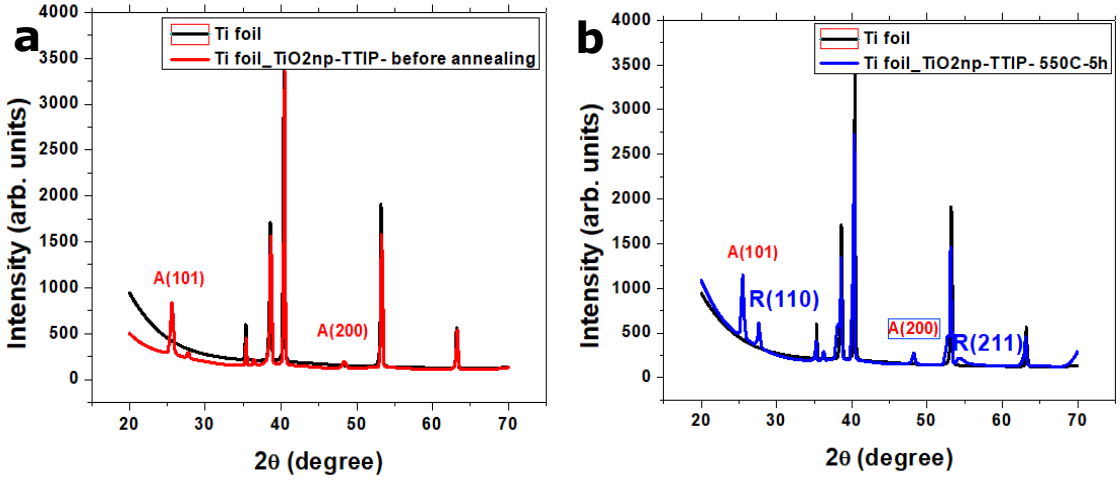

Figure 18. *XRD spectrum of the TiO_2 nanoparticles on Ti substrate (a) before annealing, and (b) after annealing at 550°C for 5 hours in the air environment.*

Chapter IV: Results and Discussion

Simulation of Beta Irradiation on TiO_2

A COMSOL model was developed to further investigate the electric field induced by SPR. Considering the example of a Pt/air interface, Figure 19 shows the difference between the stimulated electric field in a nanoporous Pt film and a smooth Pt film when a TE-mode electromagnetic wave is an incident upon the surface. The model was set up with periodic boundary conditions such that the surface conditions repeat infinitely to either side of what is shown in the simulation.

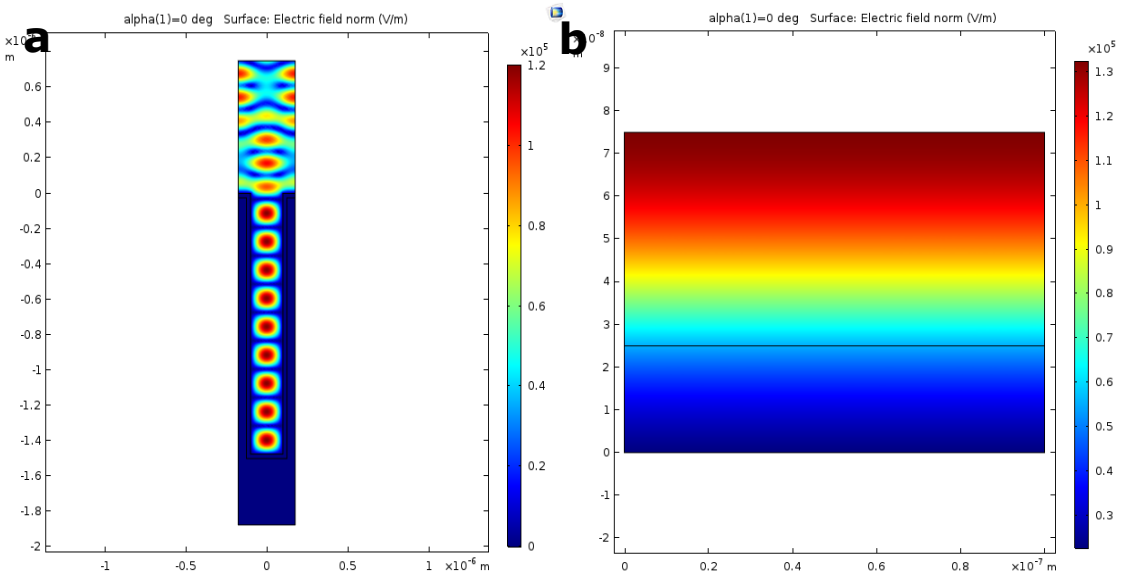

Figure 19. *COMSOL simulation results of a TE-mode electromagnetic wave incident on a Pt/TiO_2 film. (a) Porous Pt film geometry, and (b) smooth Pt film geometry. The wavelength was set to 258 nm in both cases. The pore diameter, the distance between pores, and pore depth are 250 nm, 100 nm, and 1500 nm, respectively. The thickness of the Pt film is 25 nm in both cases. The angle of incidence is 0 degrees.*

With a smooth Pt film geometry, there is virtually no electric field around the metal surface; i.e. there is no excitation of the surface plasmon-polaritons. However, the introduction of a nanoporous geometry on the Pt film leads to the formation of a highly intense electric field around the metal surface. A variation of the wavelength of the incident electromagnetic wave revealed that the wave is still capable of propagating into the pore but the intensity of the resulting electric field is reduced as shown in Figure 20. The electric field profile was very similar to the one shown in Figure 19a when the wavelengths were set to 200 and 300 nm, as they are close to the Pt/air plasmon excitation wavelength of 258 nm.

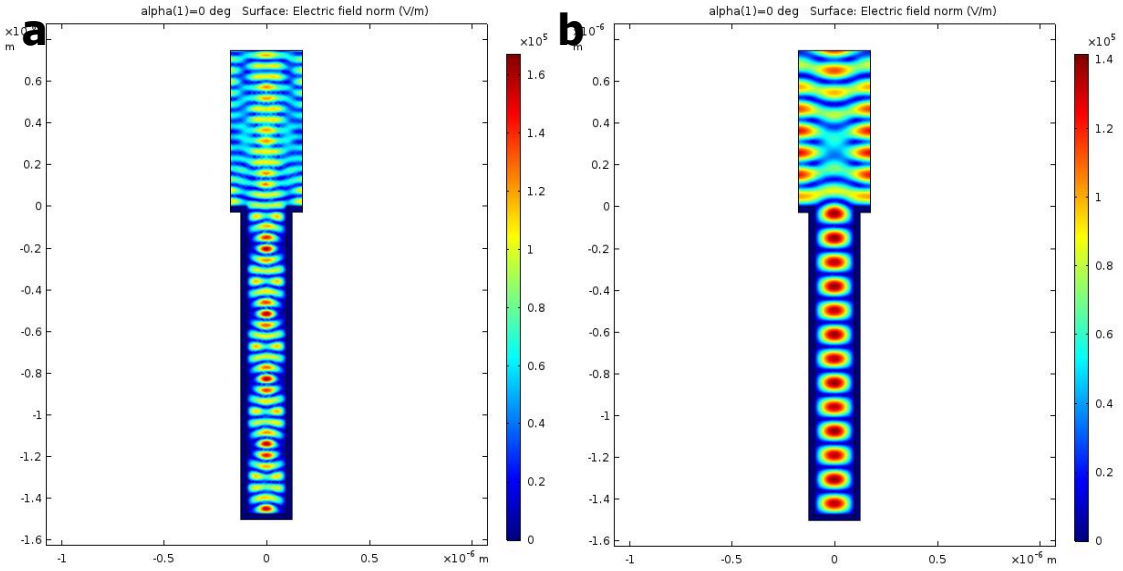

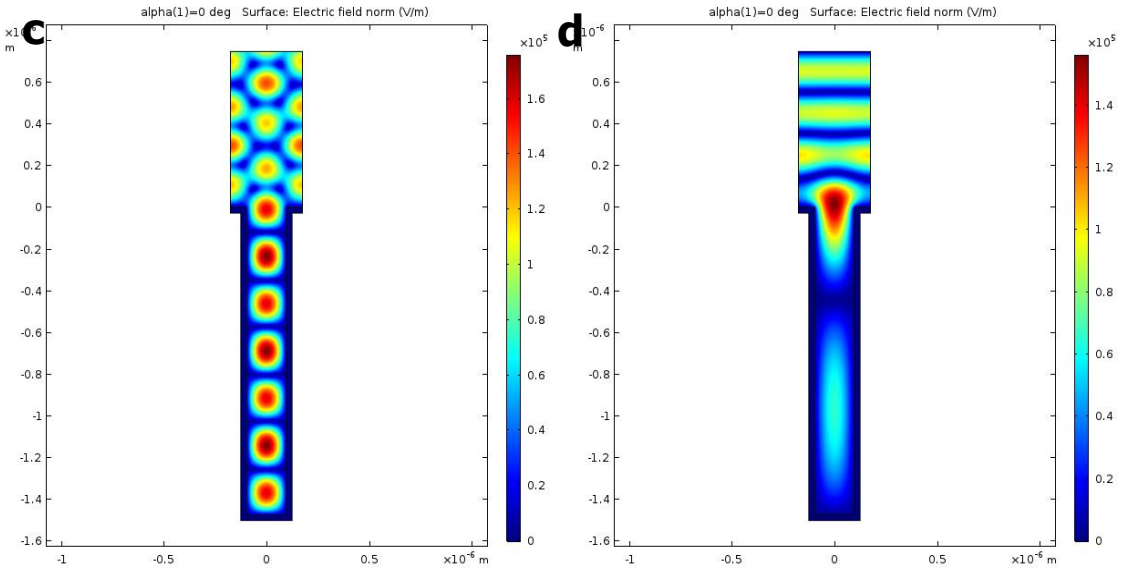

Figure 20. *COMSOL simulation results of a TE-mode electromagnetic wave incident on a Pt/ TiO_2 nanopore at a wavelength of (a) 100 nm, (b) 200 nm, (c) 300 nm, and (d) 400 nm. The pore diameter, the distance between pores, and pore depth are 250 nm, 100 nm, and 1500 nm, respectively. The thickness of the Pt film is 25 nm. The angle of incidence is 0 degrees.*

The probability of beta radiation emitted at a normal incidence can be increased by using a conformal radioactive film, such as what can be achieved by electroplating the radioactive material onto the metal surface, or by using an electron beam (a highly directional source of electrons) which is commonly used to simulate beta particle radiation.

A further variation of the model revealed that the pore diameter was an important geometrical consideration for the SPR-induced electric field (Figure 21). It was found that the optimal diameter was between 200-300 nm to produce an intense electric field within the pore. Narrow pores were shown to still produce an electric field around the top surface, but the wave did not propagate into the pore. Widening of the pores retains the propagation of the wave throughout the interior of the pore but with a diminished electric field intensity.

Besides the pore diameter, the pore depth was also considered but results showed little effect on the electric field when testing pore depths of 1-10 μm which is reasonably achievable through anodization.

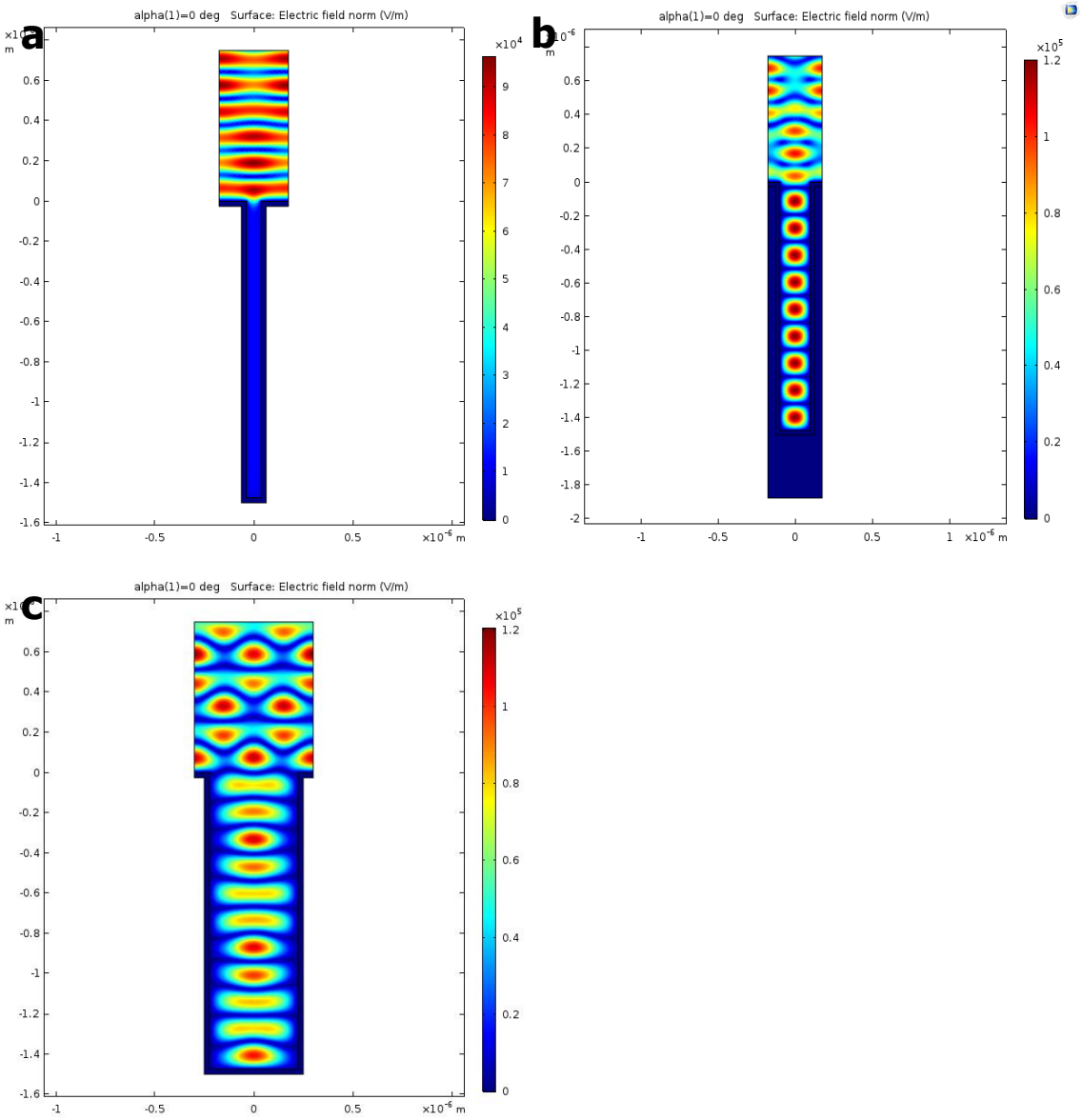

Figure 21. *COMSOL simulation results of a TE-mode electromagnetic wave incident on a Pt/ TiO2 nanopore with pore diameters of (a) 125 nm, (b) 250 nm, and (c) 500 nm. The wavelength was set to 258 nm. The pore diameter, the distance between pores, and pore depth are 250 nm, 100 nm, and 1500 nm, respectively. The thickness of the Pt film is 25 nm.*

Using experimental data from Windt. et. al.[56] and Siefke et. al.[57], the dielectric coefficients for air, Pt and TiO2 were replotted and shown in Figure 22.

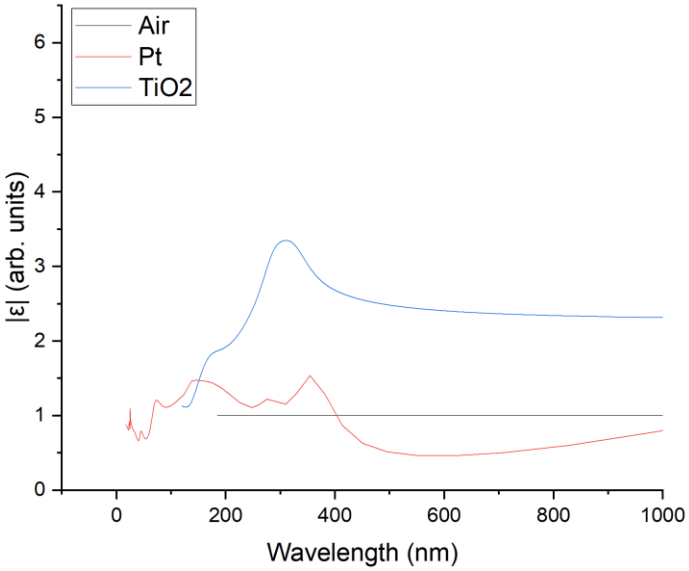

Figure 22. *Wavelength (energy) dependent dielectric constants of air, Pt, and TiO_2 materials derived from experimentally measured values*

A limiting factor to further refine the model is that most experiments and models do not test or model the dielectric properties of materials at the higher energies (low wavelengths) that might be expected in radioactive decay. Air has an approximately constant dielectric coefficient of 1 irrespective of wavelength and the first intersection with Pt occurs at a wavelength of ~66 nm. The dielectric coefficient data for TiO_2 only go as low as 120 nm, so this value was chosen for use in the following models.

The results of the COMSOL model are presented in Figure 23. After various improvements to the device fabrication procedure, we are capable of consistently producing highly ordered nanostructures with nanopore diameters ranging between 100-

150 nm, and these were chosen for testing in the simulation. From these results, it is inferred that smaller-scale nanostructures may be better suited for coupling with higher energy radiation. This is in comparison to the previous model which used a pore diameter of 250 nm and showed a poor propagation of the wave into the nanostructure at wavelengths below 200 nm.

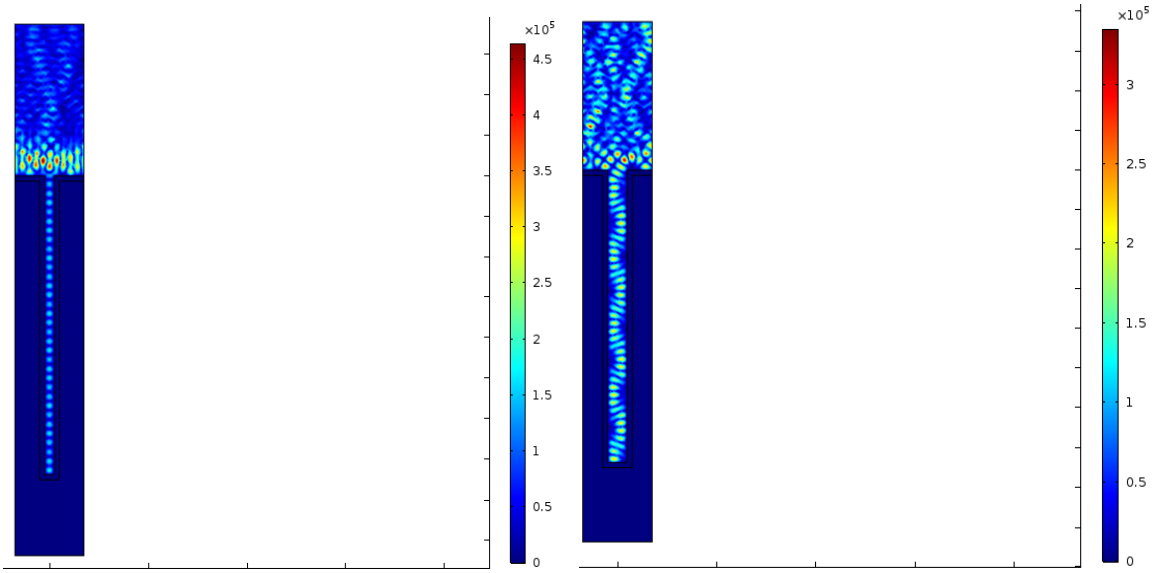

Figure 23. *COMSOL model of SPR in nanoporous Pt/TiO_2 devices with pore diameters of (left) 100 nm, and (right) 150 nm. The pore depth is 1500 nm, the thickness of Pt is 25 nm, and the wavelength was set to 66 nm (resonant condition).*

The simulations shown above consider the origin of the electromagnetic wave to be at a boundary located 1 μm above the surface of the pore. The origin of the wave was set to 15 nm above the surface for the model shown in Figure 24 to simulate a case where radioactive decay occurs in contact or very near the surface of the pore. In this model, the wave propagates all the way through to the bottom boundary of the pore, and regions of

the intense electric field are present all throughout the nanopore. Very similar results were obtained for the model having a pore diameter of 100 nm.

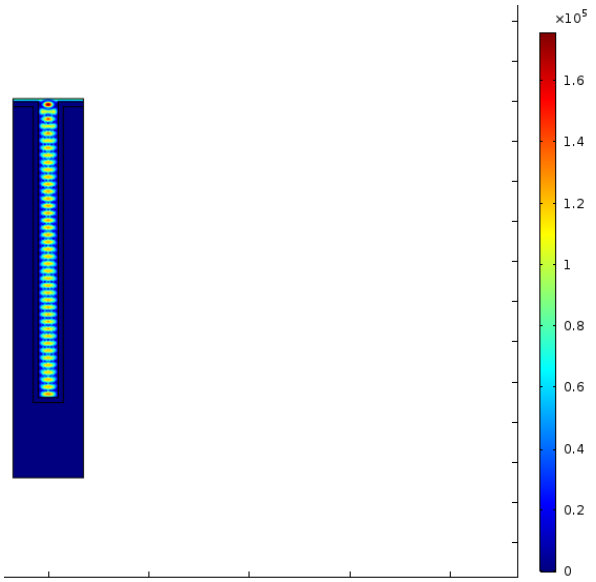

Figure 24. *COMSOL model of SPR in nanoporous Pt/TiO_2 devices with pore a diameter of 150 nm. The pore depth is 1500 nm, the thickness of Pt is 25 nm, and the wavelength was set to 66 nm (resonant condition). The origin boundary of the electromagnetic wave was placed 15 nm above the surface of the pore.*

Additional simulations were carried out using the software "monte CArlo SImulation of electroN trajectories in sOlids" (CASINO). The CASINO software uses a Monte Carlo method to track the trajectories and energies of electrons in bulk or thin-film materials. The main drawback of the software is that it is limited to planar geometries and thus it is not possible to simulate the nanoporous geometry used in the device. However, the simulation is still representative of the irradiation profile that could result from incident electrons (betas particles) on the top surface or bottom of the pores. Given that low-energy

beta particles have a higher probability of coupling with plasmons, ^{63}Ni is an excellent candidate material given its average beta energy of 17.4 keV.

Figure 25a shows the electron trajectories as a function of depth in the material and Figure 25b is the energy deposition profile. The contour lines present in Figure 25b represent the percentage of the electron energy contained in the area within; the outermost line (cyan color) contains 95% of the energy. Figure 25 (c)-(e) show the normalized distributions of electron ranges, backscattered electron energies, and backscattering angles, respectively. A Gaussian function was fit to this data resulting in an average range, backscattering energy, and backscattering angle of 765 nm, 16.4 keV, and 46.5 degrees, respectively. This suggests that the majority of electrons deposit their energy roughly halfway into the TiO_2 layer. Given that most of the backscattered electrons are close to the average beta energy of ^{63}Ni, there is a high probability that beta particles would be scattered into adjacent pores if the betas are incident upon the bottom of the pore or the pore wall and therefore improve the radioisotope energy deposition.

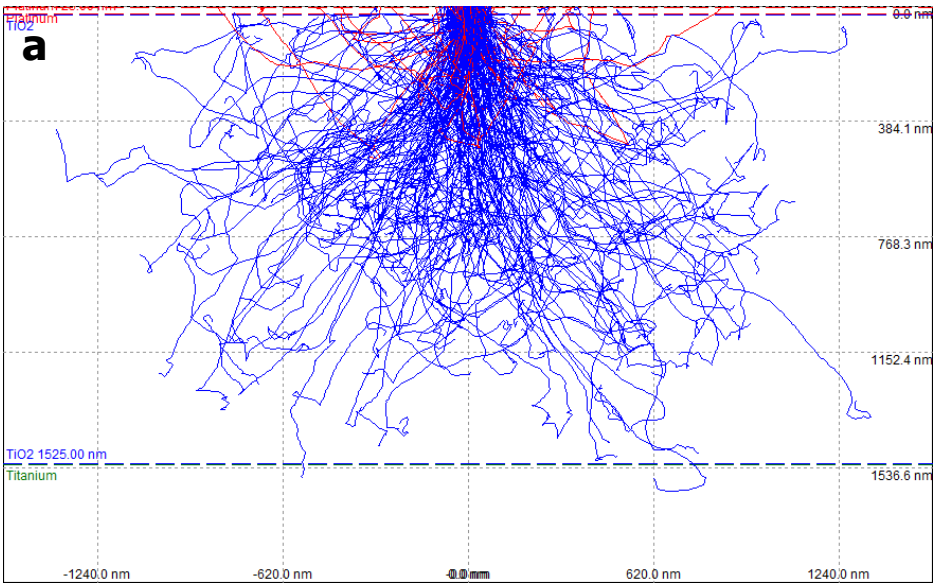

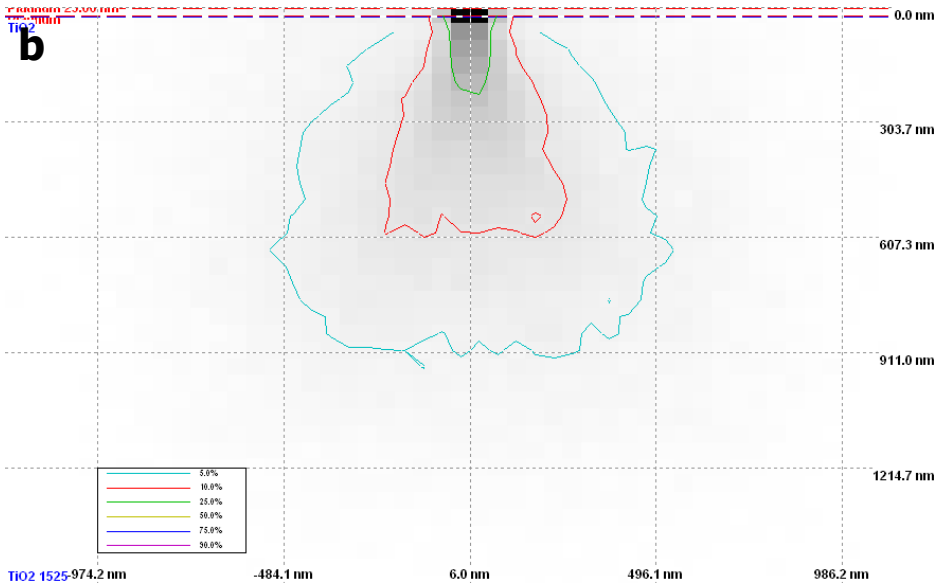
b
TiO2
0.0 nm
303.7 nm
607.3 nm
911.0 nm
1214.7 nm
5.0%
10.0%
25.0%
50.0%
75.0%
90.0%
TiO2 1525
-974.2 nm
-484.1 nm
6.0 nm
496.1 nm
986.2 nm

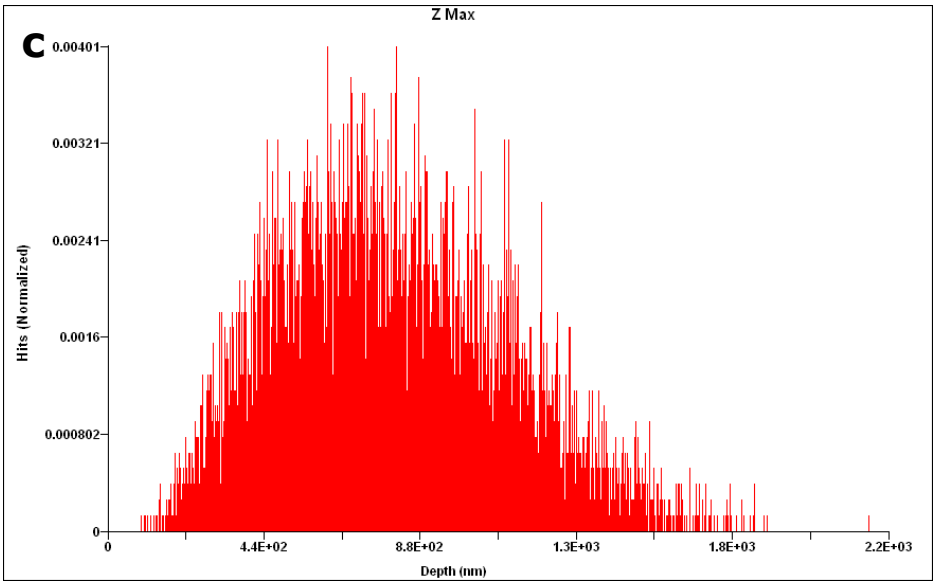
c
Z Max
Hits (Normalized)
0.00401
0.00321
0.00241
0.0016
0.000802
0
0
4.4E+02
8.8E+02
1.3E+03
1.8E+03
2.2E+03
Depth (nm)

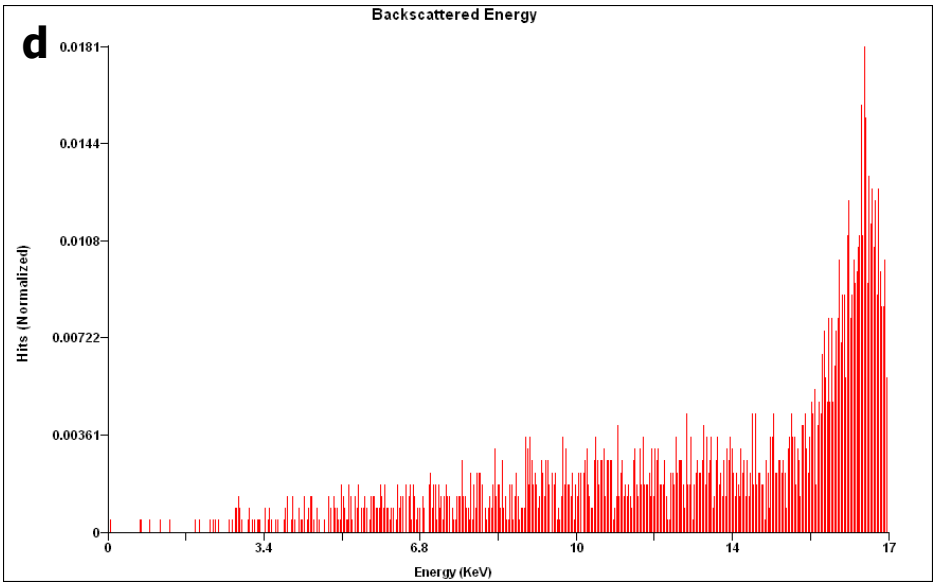
d
Backscattered Energy
Hits (Normalized)
0.0181
0.0144
0.0108
0.00722
0.00361
0
0
3.4
6.8
10
14
17
Energy (KeV)

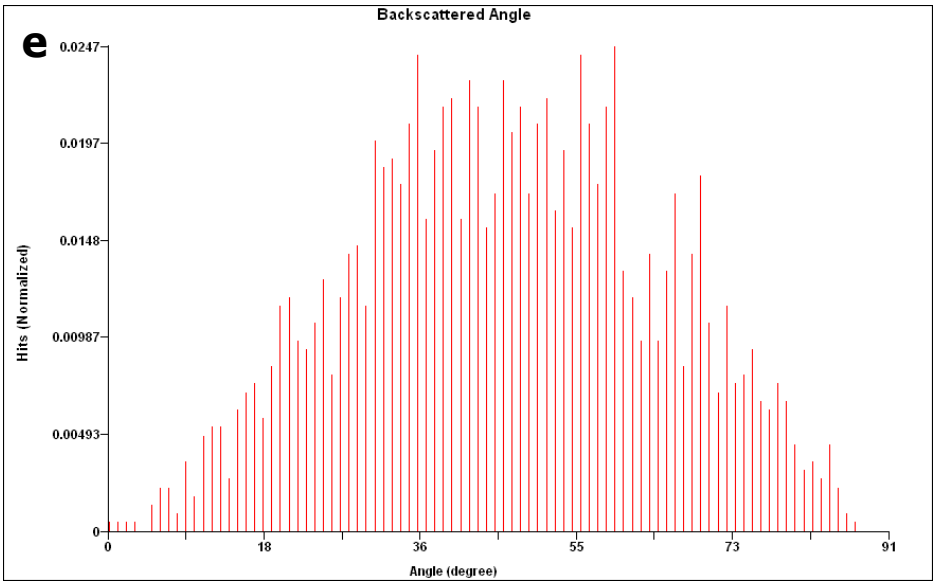

Figure 25. *CASINO simulation of 17 keV electrons on a Pt/TiO_2/Ti surface showing (a) electron trajectories, (b) energy deposition profile, (c) range distribution of electrons, (d) distribution of backscattered electrons energies, and (e) distribution of angles of backscattered electrons. The simulation consisted of 10,000 electrons as a Gaussian beam having a radius of 10 nm. The film thicknesses were 25 nm, 1,500 nm, and 32,000 nm for Pt, TiO_2, and Ti, respectively.*

The thickness of the Schottky metal (Pt) has a direct effect on the I-V properties of the Schottky diode. However, the thickness of the Schottky metal also affects the irradiation profile as it is generally the first layer to interact with incident radiation. The same model as used above was modified to have Pt film thicknesses ranging from 25 nm to 300 nm, which can be produced by either ALD or sputtering processes. The greatest effect of the Pt film thickness on the irradiation profile was in 1) the average range of electrons, 2) the radial scattering distance (i.e. the distance electrons scatter from the beam centerline), and 3) the backscattering coefficient (Figure 26). At Pt film thicknesses greater than 200 nm, it was found that the majority of electrons were depositing their energy within the Pt film with only about 30-40% reaching the TiO_2 layer beyond. Furthermore, the

backscattering coefficient increased rapidly with increasing Pt film thickness, reaching a plateau around 200 nm at which point nearly half of electrons are backscattered. The radial scattering distribution showed an inverse proportionality with the increasing Pt film thickness and plateauing around 100 nm thickness. This is potentially due to a greater amount of electrons continuing on into the TiO_2 layer since there is less backscatter and increasing the scattering probability in this layer. The backscattering energy distributions and backscattering angles skewed towards lower values but to a minimal degree. Overall, these simulation results show that the Schottky metal thickness needs to be carefully controlled in order to improve the radioisotope energy coupling.

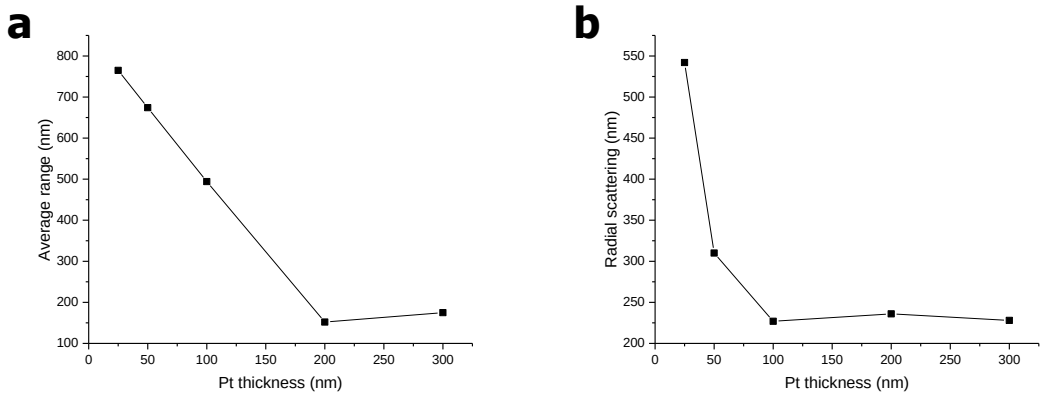

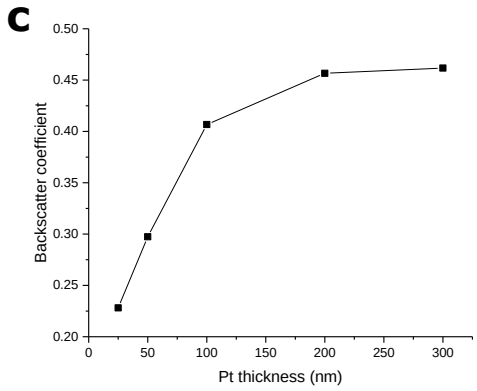

Figure 26. *CASINO simulation of 17 keV electrons on a Pt/TiO_2/Ti surface showing (a) average electron range, (b) radial scattering, and (c) backscatter coefficient at various Pt film thicknesses. The simulation consisted of 10,000 electrons as a Gaussian beam having a radius of 10 nm. The film thicknesses were 25 nm, 1,500 nm, and 32,000 nm for Pt, TiO_2, and Ti, respectively.*

Effects of Beta Radiation on Barrier Height in Nanoporous Pt/TiO_2 Schottky Diodes

Several Pt/TiO_2/Ti Schottky diodes were fabricated using the methodology described earlier. The diodes were exposed to a ^{63}Ni source that was fabricated by depositing a solution of $^{63}NiCl_2$ in diluted HCl via a precision micropipette onto a 3D-printed acrylic piece with an area of 1.2 cm^2 and allowed to dry naturally. The total activity deposited was 20 mCi with an estimated effective activity of 10 mCi. The measurements involving the radioisotope source were conducted in a pressure-controlled glovebox. A summary of the device fabrication conditions is presented in Table 1. The I-V measurements of the devices when exposed to the radioisotopes are shown in Figure 27.

Table 1. *Summary of Pt/TiO_2/Ti Schottky diode fabrication conditions.*

Sample	Oxide condition	Annealing Temperature (°C)	Annealing time (h)	ALD cycles
(a)	Anodized + annealed	450	5	20
(b)	Anodized + annealed	450	5	30
(c)	Annealed only	450	5	20
(d)	Annealed only	450	5	30
(e)	Annealed only	550	5	50

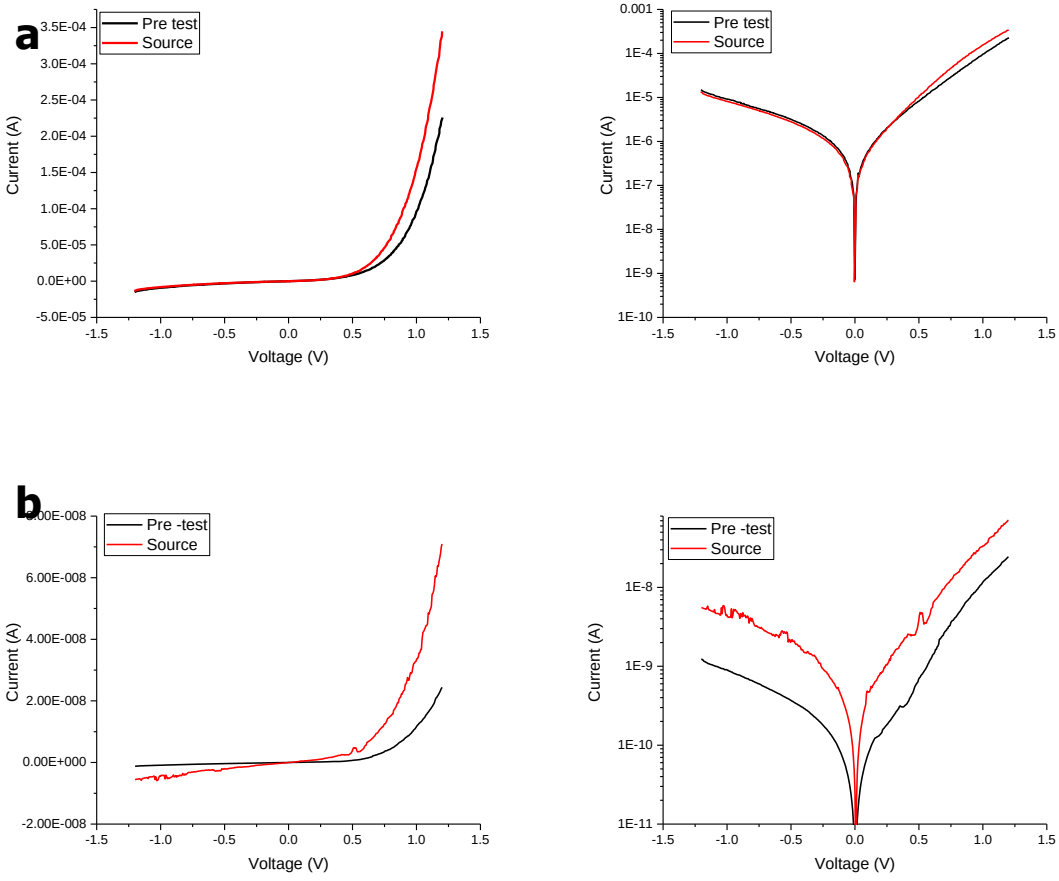

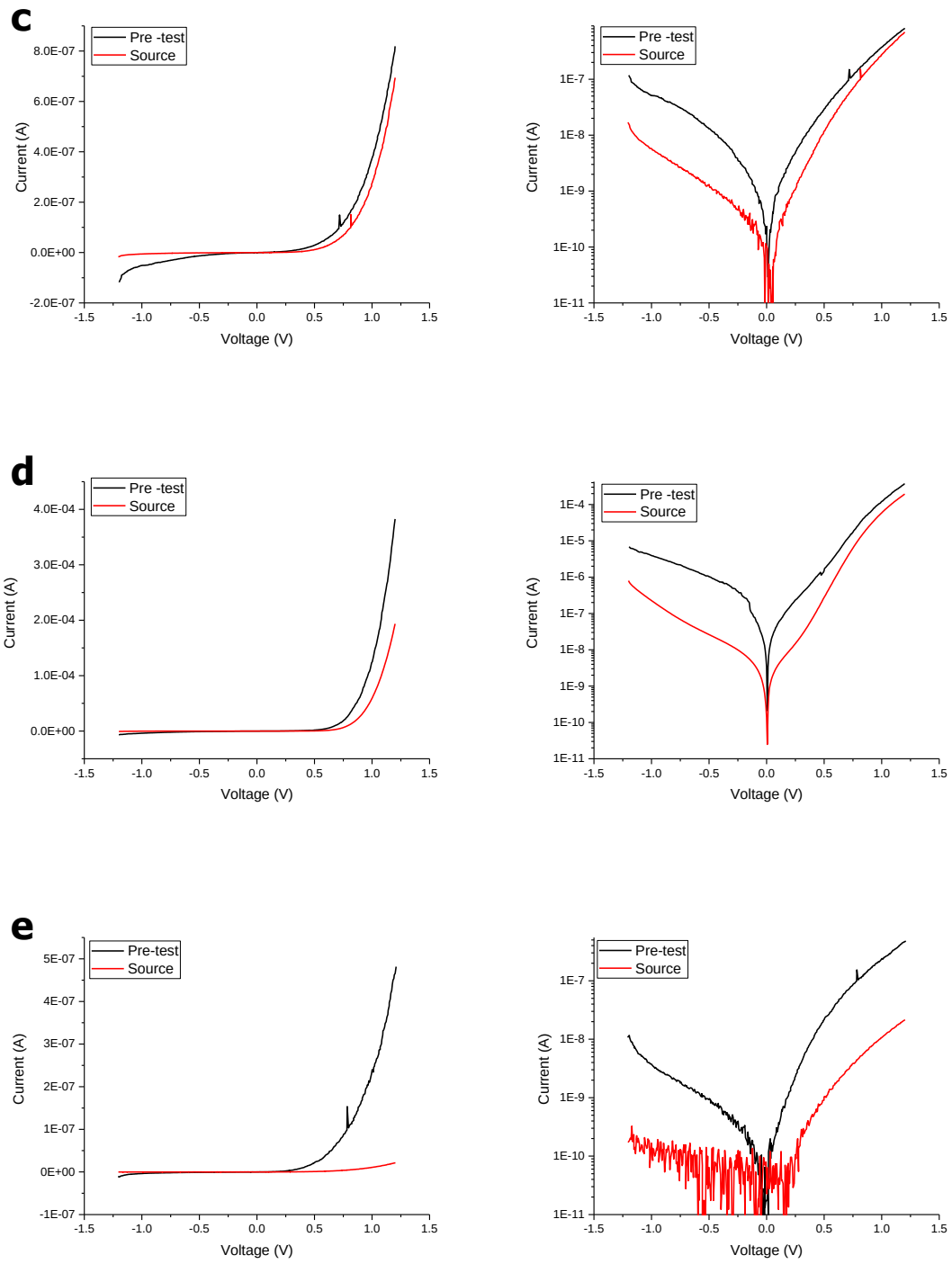

Figure 27. *I-V measurements of Pt/TiO_2/Ti Schottky diodes with corresponding semi-log plots. Sample conditions are summarized in Table 1. All measurements were performed in an atmosphere controlled glovebox using a Keithley 2601A Sourcemeter.*

All of the devices in Figure 27 show a change in the current response when exposed to the radioisotope. It is observed as a general trend that anodized (nanoporous) samples exhibit an increase in the forward bias current resulting from a shift in the turn-on voltage to a lower value. Contrarily, the turn-on voltage in annealed only (planar) samples shifts towards a higher value and results in a reduction of the forward bias current. However, the planar samples also show a significant reduction in the leakage current. The change in current during exposure to the radioisotope is a result of a lowering (in the case of a current increase) or heightening (in the case of a current decrease) of the barrier height. The barrier height was calculated by first fitting the measured data to Equation (14) that expresses the I-V characteristic of a diode in the thermionic emission conduction regime[58]. The data fitting was done using a Levenberg-Marquardt curve fitting algorithm to obtain the parameters of interest.

$$I \approx I_0 \exp\left(\frac{V - IR_s}{n\frac{kT}{q}}\right) \quad \textbf{(14)}$$

where I is the measured current, I_0 is the saturation current, V is the applied voltage, R_s is the series resistance, n is the diode ideality factor, k is the Boltzmann constant, T is the temperature, and q is the electron charge. From the data fit, it was possible to determine the saturation current which was then used to calculate the barrier height ϕ_b by solving for it in Equation (15).

$$I_0 \approx a\, A^{**}\, T^2 \exp\left(\frac{-\phi_b}{kT}\right) \quad \textbf{(15)}$$

where a is the diode area, and A^{**} is the effective Richardson constant of the semiconductor (1200 A cm^{-2} K^{-2} for n-type TiO_2)[59]. The change in barrier height $\Delta\phi_b$ was calculated with Equation (16).

$$\Delta\phi_b = \phi_{b,Radioisotope} - \phi_{b,Non-radioisotope} \quad \textbf{(16)}$$

$$\Delta\phi_b < 0 \rightarrow barrier\ height\ lowering$$

$$\Delta\phi_b > 0 \rightarrow barrier\ height\ increasing$$

A summary of the barrier height changes for each of the devices is presented in Table 2.

Table 2. *Summary of measured current response of Pt/TiO_2/Ti Schottky diodes during exposure to radioisotope source. The current change factor was calculated as the ratio of the current at ±1.2 V before and after exposure to the radioisotope. A "negligible" change means the ratio is ~1.*

Sample	Observed effect on current	Forward bias current change factor	Reverse bias current change factor	Barrier height before/during source exposure	Change in barrier height $\Delta\Phi_b$ (eV)
(a)	Forward bias current increase	1.5	Negligible	0.835±0.016 / 0.820±0.030	-0.015±0.046
(b)	Forward & reverse bias current increase	3	4.5	1.063±0.037 / 1.026±0..025	-0.038±0.061
(c)	Reverse bias current decrease	Negligible	0.1	0.973±0.028 / 0.998±0.033	+0.026±0.061
(d)	Forward & reverse bias current decrease	Negligible	0.1	0.867±0.046 / 0.898±0.061	+0.031±0.107
(e)	Forward & reverse bias current decrease	Negligible	0.02	0.974±0.034 / 1.056±0.033	+0.081±0.067

The large differences in the barrier heights from device to device given in Table 2 are likely a consequence of nano- to microscale surface defects that form during sample processing. The thin Ti foils used to fabricate the Schottky diodes were chosen so as to reduce the recombination rate of EHPs generated by the incident beta radiation. However, the thin Ti foils which are initially highly flexible become more rigid after the annealing step, and any curvature present on the sample prior to annealing is accentuated after this process, resulting in the formation of cracks in the TiO_2 layer. This has been observed to occur to a greater extent in the 32-μm Ti foils.

The presence of these defects has a significant effect on the electrical characteristics of the Schottky diodes, as these surface inhomogeneities can lead to a lowering of the barrier height in localized regions. In a study performed by Bhatnagar et. al.[60] on surface inhomogeneities of SiC Schottky diodes, it was found that the electrical characteristics were affected by the size (area relative to the total diode area) of the inhomogeneities, but more importantly by the barrier height in these localized regions. Even when the inhomogeneities were small in size, a localized barrier height lowering of 0.1 eV could increase the ratio of the defect current to that of the ideal diode current (i.e. defect-free) from 10^1 to 10^3. As the difference between the defect barrier height and the ideal barrier height increases, the reverse bias leakage current flows almost entirely through the defective region with minimal contribution from the high barrier height region. In contrast, the Schottky barrier height inhomogeneities were found to have a negligible impact on the forward I-V characteristics except at small biases.

The cases where exposure to the radioisotope only results in an increase of the forward bias current can be understood based on charge multiplication. Here, the incident beta radiation results in the production of hot electrons by providing the energy to allow the transition from the valence band to the conduction band in the Pt layer as well as band-to-band excitation in the TiO_2 layer. Furthermore, the highly energetic beta radiation can produce many secondary electrons through impact ionization. The beta radiation-induced lowering of the Schottky barrier facilitates the conditions such that these secondary electrons can contribute to the total current. Samples that showed an increase to both the forward and the reverse bias current likely still exhibit charge multiplication, but the beta radiation may also aggravate surface inhomogeneities and cause an increase in the leakage current.

Device Improvements by Two-step anodization and Rapid Thermal Annealing

An issue with the previous devices was the uniformity of electrical characteristics throughout the sample surface as well as reliability from device to device. To address this problem, the fabrication process was changed from single anodization to a two-step anodization process. Two-step anodizing consists of initial anodization of the substrate followed by ultrasonication to remove the nanoporous film that is produced. In general, the nanoporous film that is created during the first anodization can contain surface defects that arise as a result of an inhomogeneous electric field present on the sample during this initial step. Defects are removed during the ultrasonication step and a template is left for the

nanotubes to grow during the second anodization step. This results in the formation of highly ordered TiO_2 nanotubes with a surface that is defect-free.

In addition to the introduction of two-step anodization to the device fabrication process, the electrical characteristics of the devices were significantly improved using Rapid Thermal Annealing (RTA). This is a post-processing method that has been used in the semiconductor industry for more than two decades and was originally developed for the activation of dopants and the interfacial reaction of metal contacts but has since been used for a wider range of applications such as oxide growth and chemical vapor deposition[61]. The use of RTA has become increasingly critical for semiconductor processing as transistor geometries continue to reduce in size and require shorter annealing durations to retain a small junction size[62].

In essence, the RTA process consists of heating a substrate from ambient temperature to high temperatures ranging from approximately 700 K to 1500 K followed by a fast and controlled cooling step. The required temperature for the RTA process is dependent upon the materials being used – i.e. the activation energy for dopants or interfacial materials. A typical RTA system uses infrared lamps in order to heat the substrate material and the temperature is determined by an indirect sensor. In our lab, the RTA process was performed using a modified quartz tube furnace with a schematic of the system shown in Figure 28.

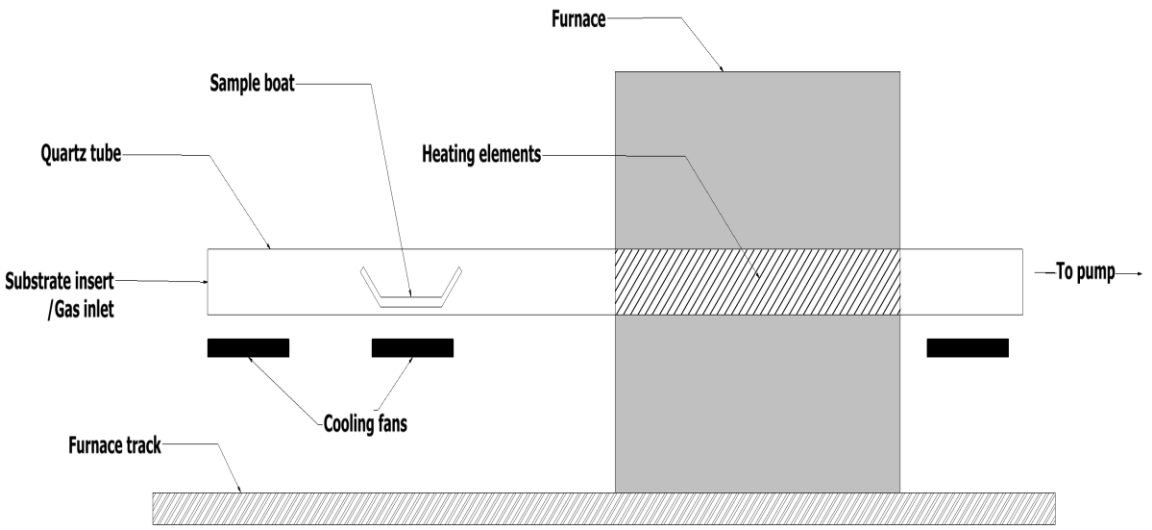

Figure 28. *Schematic diagram of RTA system*

The samples are placed in a boat and introduced into the quartz tube. The tube is evacuated using a mechanical pump to achieve a low vacuum followed by the introduction of N_2 gas. Cooling fans are active throughout the process to maintain the samples at room temperature while the desired RTA temperature is reached in the furnace. Once the RTA temperature has been achieved, the furnace is moved to cover the samples to perform the annealing for the desired amount of time. Finally, the furnace is moved away from the samples and the fans begin cooling the samples back to room temperature.

The measured electrical characteristics of samples fabricated using both the two-step anodization process as well as the RTA process are shown in Figure 29. The processing parameters for these samples are presented in Table 3.

Table 3. *Processing parameters for two-step anodized and RTA treated samples*

Parameter	Value	Unit

1st & 2nd anodization current	50	mA
1st & 2nd anodization voltage	60	V
1st and 2nd anodization time	60	minutes
Ultrasonication time	30	minutes
Annealing temperature	450	°C
Annealing time	5	hours
ALD Pt	50	cycles
RTA processing temperature	650	°C
RTA processing time	90	seconds
RTA N_2 pressure	25	mTorr

a

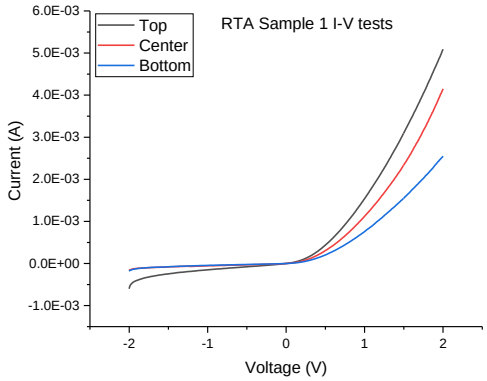

b

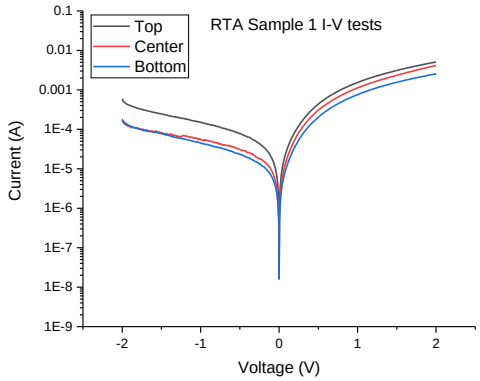

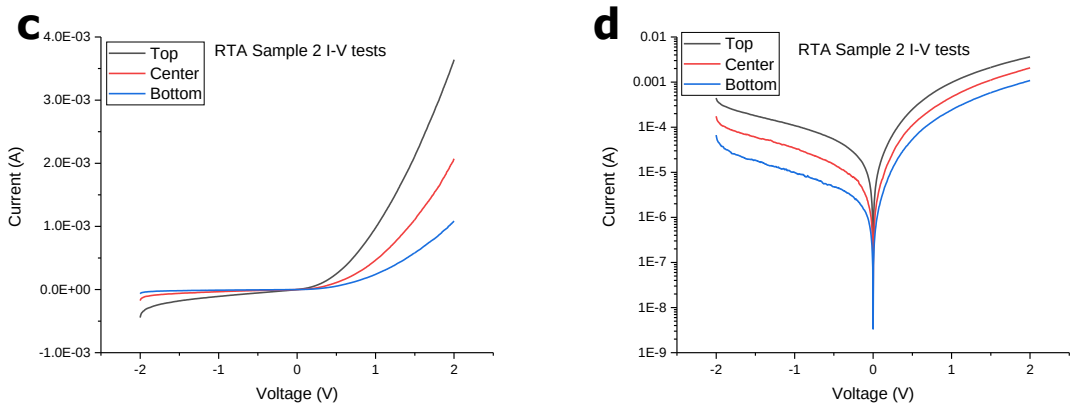

Figure 29. *I-V characteristics of samples fabricated using two-step anodization and treated through RTA. (a, b) RTA sample 1 with corresponding semilog scale plot, and (c, d) RTA sample 2 with corresponding semilog scale plot. Measurements were taken using a Keithley 2601A sourcemeter under dark conditions.*

There are various improvements that can be observed in the devices shown in Figure 29 compared to those shown in Figure 27. The RTA treated samples exhibit forward bias currents in the milliamp range which is 10^3 to 10^5 times higher than the previously fabricated devices. This dramatic increase in the current is a consequence of diffusion and interfacial reactions at the Pt/TiO_2 interface and results in a more stable contact. The breakdown voltage is increased to approximately -2V compared to the previous -1.2V. Furthermore, both RTA treated samples exhibit good uniformity of the electrical properties across the sample surface with all three of the measurement locations showing similar levels of current. The new fabrication method also shows improvements in the consistency and reliability from device to device as both samples show very similar I-V characteristics.

Recent studies have shown that RTA can also be used to produce a crystalline phase of TiO_2[63,64]. This was confirmed by performing XRD on the samples at each stage of the device fabrication process (Figure 30).

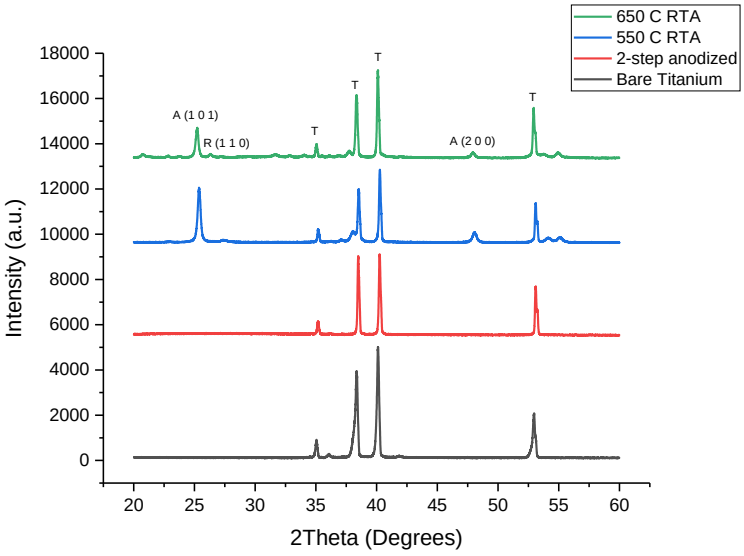

Figure 30. *XRD spectra of RTA treated TiO_2 samples. The RTA treatment time was 10 minutes at the specified temperature in a 25 mTorr N_2 environment.*

While both of the tested processing temperatures showed similar results, the samples treated at 650°C suffered from delamination of the anodized film after the RTA process. Thus, an RTA treatment temperature of 550°C seems to be ideal as it did not cause any delamination of the anodized film and it produced a full anatase crystalline phase which is more favorable to produce a Schottky diode compared to rutile TiO_2 or mixed-phase TiO_2. From a fabrication standpoint, this represents a significant improvement as the previous annealing step was the most time-consuming process requiring 10-12 hours due to the slow temperature ramping, holding at temperature, and slow cooling. Using the RTA

process to obtain a crystalline phase of TiO_2 reduces the total device fabrication time from three to four days down to one to two days.

The RTA-treated samples were also tested under beta radiation exposure and also exhibited a current amplification response while exposed to the radioisotope (Figure 31).

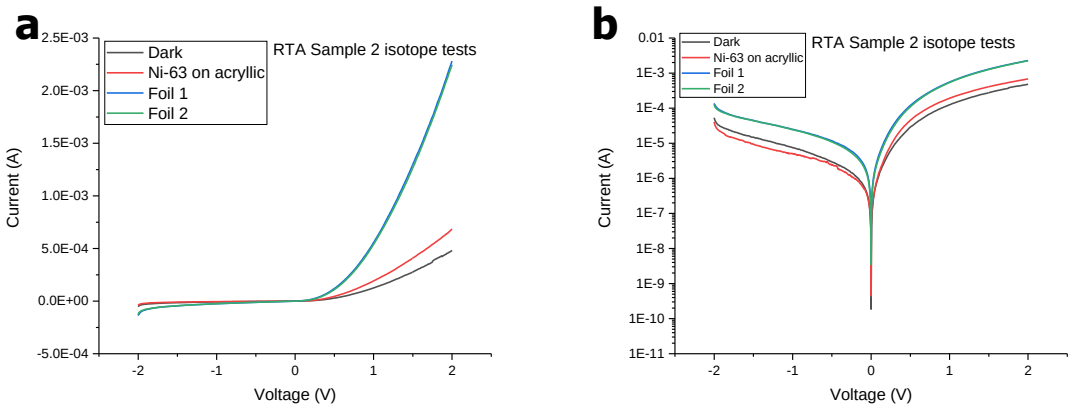

Figure 31. *I-V measurements of RTA treated TiO_2 Schottky diodes before and during ^{63}Ni beta radiation exposure. (a) I-V characteristics and (b) corresponding semilog scale plot. Measurements were performed in a controlled environment glove box. Measurements were taken using a Keithley 2601A sourcemeter. RTA sample 1 was damaged while loading into the glove box and could not be measured.The total activity of each of the ^{63}Ni foils was 15 mCi and the total activity of the ^{63}Ni deposited on acrylic was 20 mCi.*

The RTA treated device showed a current amplification during all the radioisotope exposure tests and was most significant when the device was exposed to the ^{63}Ni foils. A summary of the current response and effects of the radiation on the barrier height is given in Table 4.

Table 4. *Summary of current response of RTA treated TiO_2 Schottky diodes before and during radiation exposure. The current change factor was calculated at ±2 V.*

Isotope used	**Forward bias current change factor**	**Reverse bias current change factor**	**Barrier height before/during source exposure (eV)**	**Change in barrier height $\Delta\Phi_b$ (eV)**
^{63}Ni on acrylic	1.4	Negligible	0.723±0.026 / 0.713±.025	-0.010±0.052
^{63}Ni foil 1	4.7	Negligible	0.723±0.026 / 0.683±.031	-0.040±0.058
^{63}Ni foil 2	4.7	Negligible	0.723±0.026 / 0.684±.033	-0.039±0.060

The current response and derived values of the Schottky barrier height shown in **Table 4** are consistent with the devices fabricated previously wherein a lowering of the Schottky barrier height results in a current amplification in the device by facilitating radio-excited hot and secondary electrons to overcome the charge barrier and contribute to the total current. However, the RTA treated samples show a greater current amplification than nearly all of the previous samples owing to the improved contact produced by the RTA treatment.

A comparison of the effects of beta radiation on the device barrier heights is shown in Figure 32. This data makes it clear that the Schottky barrier lowering only occurs in the devices where nanostructures are present and provide some evidence for the surface plasmon interaction. Conversely, it is observed that in the absence of nanostructures the beta radiation seems to produce a semi-insulating effect by increasing the barrier height. However, the phenomena causing this barrier height increase are not fully understood at this time.

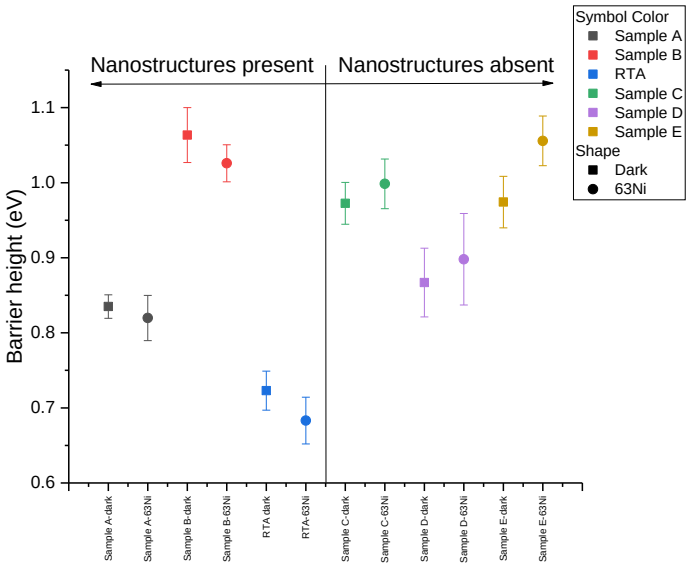

Figure 32. *Effect of beta radiation on Schottky barrier height for nanoporous Pt/TiO_2 devices. All devices with nanostructures present exhibit a decrease of the barrier height when exposed to radiation while devices with nanostructures absent exhibit an increase of the barrier height.*

Chapter V: Conclusion

Summary

Experimental and simulation work was done to explore the possibility of using the phenomena of surface plasmon resonance to improve the energy coupling of transistors with radioisotopes.

Simulations of beta radiation interacting with a $Pt/TiO_2/Ti$ Schottky diode were performed using COMSOL and CASINO. The COMSOL simulation showed the formation of an intense electric field around the Pt metal film that was dependent upon incident wavelength/energy, and geometrical parameters such as wave angle of incidence and pore diameter. The CASINO simulation showed a strong dependence of the electron/beta irradiation profile on the thickness of the Pt film.

Nanoporous $Pt/TiO_2/Ti$ Schottky diodes were fabricated and tested under radioisotope exposure. The measurements showed that the devices under test either exhibited an increase to the forward bias current or a decrease to the leakage current that occur as a result of beta radiation-induced lowering or heightening of the Schottky barrier height, respectively. The increase to the forward bias current can be explained by charge multiplication wherein radio-excited electrons generate secondary electrons before thermalization and exploit the lower barrier height to produce a higher total current.

Implications and Future Work

In terms of device fabrication, some work is still needed to find the optimal anodizing, RTA, and ALD conditions to minimize the leakage current in the device. It is suggested that a primary focus be given to finding the proper RTA temperature and treatment time as the introduction of RTA into the fabrication process yielded the most significant improvements to the device.

It is also necessary to further refine the surface plasmonic model to find more concrete proof of plasmonic excitation and resonance with beta radiation. While the current work provides some evidence for the occurrence of this phenomenon, it was not possible to determine a definitive causal relationship.

This research is meant to lay the foundation for the development of a low-cost and portable radiation detector. In its current state, the nanoporous TiO_2/Pt Schottky device can produce a sizeable amplification of the current when exposed to radiation. The radiation-induced current response in the device occurs even with weak beta radiation such as that emitted from ^{63}Ni which would normally require scintillation equipment to be detected. Due to limitations in the availability of radioisotopes in our laboratory, it was not possible to test the device with other forms of radiation, such as alpha or gamma radiation, but testing performed with higher energy radiation emitted from $^{90}Sr/^{90}Y$ shows that there is a proportionality between the current amplification in the device and the energy of the incident radiation. This suggests that the device has the potential to detect alpha and gamma radiation as well.

References

1. Knoll, G. F. *Radiation Detection and Measurement*. (Wiley, 2010). doi:10.4274/nts.018.

2. Ben Amor, S., Rogier, B., Baud, G., Jacquet, M. & Nardin, M. Characterization of zirconia films deposited by r.f. magnetron sputtering. *Mater. Sci. Eng. B* **57**, 28–39 (1998).

3. Patel, U. S., Patel, K. H., Chauhan, K. V., Chawla, A. K. & Rawal, S. K. Investigation of Various Properties for Zirconium Oxide Films Synthesized by Sputtering. *Procedia Technol.* **23**, 336–343 (2016).

4. Gai, G. *et al.* Facile electrospinning fabrication of nickel oxide nanotubes and their photocatalytic properties. *J. Mater. Sci. Mater. Electron.* **28**, 7271–7276 (2017).

5. Amin, S. *et al.* Functional Nickel Oxide Nanostructures for Ethanol Oxidation in Alkaline Media. *Electroanalysis* **32**, 1052–1059 (2020).

6. Bharathan, P. Investigation of Properties of AsxSe1−x Thin Films for Direct Conversion. *J. Electron. Mater.* **44**, 2725–2735 (2015).

7. Yang, W. *et al.* NiO nanorod array anchored Ni foam as a binder-free anode for high-rate lithium ion batteries. *J. Mater. Chem. A* **2**, 20022–20029 (2014).

8. Yan, X. *et al.* Synthesis of hollow nickel oxide nanotubes by electrospinning with structurally enhanced lithium storage properties. *Mater. Lett.* **136**, 74–77 (2014).

9. Nakano, Y. Ultra-high efficiency photovoltaic cells for large scale solar power generation. *Ambio* **41**, 125–131 (2012).

10. Yu, J. S. & Ko, Y. H. Metal-oxide semiconductor nanostructures for energy and sensing applications. *SPIE Photonics West 2014-OPTO Optoelectron. Devices Mater.* **8987**, 89871G (2014).

11. Devan, R. S., Patil, R. A., Lin, J. H. & Ma, Y. R. One-dimensional metal-oxide nanostructures: Recent developments in synthesis, characterization, and applications. *Adv. Funct. Mater.* **22**, 3326–3370 (2012).

12. Park, J., Heo, J. K. & Kang, Y. C. The properties of RF sputtered zirconium oxide thin films at different plasma gas ratio. *Bull. Korean Chem. Soc.* **31**, 397–400 (2010).

13. Greiner, M. T. & Lu, Z.-H. Thin-film metal oxides in organic semiconductor devices: their electronic structures, work functions and interfaces. *NPG Asia Mater.* **5**, e55 (2013).

14. Kong, D., Seo, C., Kim, B., Cho, C. S. & Lee, J. Air-bridge-type electrodes for high-efficiency photovoltaic cell. *Micro Nano Lett.* **6**, 546–548 (2011).

15. Schoen, K. J., Woodall, J. M., Cooper, J. A. & Melloch, M. R. Design considerations and experimental analysis of high-voltage SiC Schottky barrier rectifiers. *IEEE Trans. Electron Devices* **45**, 1595–1604 (1998).

16. Hoang, K. N., Kim, H. T., Jun, W. & Park, C. Epitaxial gallium nitride thin films grown on silicon substrates utilizing gallium nitride seed-layer formed by liquid source precursor. *Korean J. Chem. Eng.* **29**, 130–133 (2012).

17. Hang, R. *et al.* Fabrication of Ni-Ti-O nanotube arrays by anodization of NiTi alloy and their potential applications. *Sci. Rep.* **4**, 21–24 (2014).

18. Maznev, A. A. & Wright, O. B. Demystifying umklapp vs normal scattering in lattice thermal conductivity. *Am. J. Phys.* **82**, 1062–1066 (2014).

19. Atyaoui, M. *et al.* Enhancement in photovoltaic properties of silicon solar cells by surface plasmon effect of palladium nanoparticles. *Superlattices Microstruct.* **92**, 217–223 (2016).

20. Kim, B. H. & Kwon, J. W. Plasmon-assisted radiolytic energy conversion in aqueous solutions. *Sci. Rep.* **4**, (2014).

21. Khan, M. R., Chuan, T. W., Yousuf, A., Chowdhury, M. N. K. & Cheng, C. K. Schottky barrier and surface plasmonic resonance phenomena towards the photocatalytic reaction: study of their mechanisms to enhance photocatalytic activity. *Catal. Sci. Technol.* **5**, 2522–2531 (2015).

22. Zhou, L. *et al.* Self-assembly of highly efficient, broadband plasmonic absorbers for solar steam generation. *Sci. Adv.* **2**, (2016).

23. Agrawal, A., Kriegel, I. & Milliron, D. J. Shape-dependent field enhancement and plasmon resonance of oxide nanocrystals. *J. Phys. Chem. C* **119**, 6227–6238 (2015).

24. Zhang, X., Zhao, J., Wang, S., Dai, H. & Sun, X. Shape-dependent localized surface plasmon enhanced photocatalytic effect of ZnO nanorods decorated with Ag. *Int. J. Hydrogen Energy* **39**, 8238–8245 (2014).

25. Nehl, C. L. & Hafner, J. H. Shape-dependent plasmon resonances of gold nanoparticles. *J. Mater. Chem.* **18**, 2415–2419 (2008).

26. Pitarke, J. M., Silkin, V. M., Chulkov, E. V. & Echenique, P. M. Theory of surface

plasmons and surface-plasmon polaritons. *Reports Prog. Phys.* **70**, 1–87 (2007).

27. Guo, D., Xie, G. & Luo, J. Mechanical properties of nanoparticles: basics and applications. *J. Phys. D. Appl. Phys.* **47**, 013001 (2014).

28. Gong, S. *et al.* Electron beam excitation of surface plasmon polaritons. **22**, 1176–1181 (2014).

29. Cai, W., Sainidou, R., Xu, J., Polman, A. & Garcı, F. J. Efficient Generation of Propagating Plasmons by Electron Beams. (2009).

30. Bashevoy, M. V *et al.* Generation of Traveling Surface Plasmon Waves by Free-Electron Impact. (2006).

31. Zhang, Y., Hu, M., Yang, Y., Zhong, R. & Liu, S. Terahertz radiation of electron beam – cylindrical mimicking surface plasmon wave interaction. (2009) doi:10.1088/0022-3727/42/4/045211.

32. Kumar, P., Kumar, R. & Kumar, S. Cherenkov terahertz surface plasmon excitation by an electron beam over an ultrathin metal film. *J. Appl. Phys.* **223101**, 1–5 (2017).

33. Mirzaei, Y., Rostami, G., Dolatyari, M. & Rostami, A. Investigation of efficient mathematical permittivity modeling for modal analysis of plasmonics layered structures. *Optik (Stuttg).* **126**, 323–327 (2015).

34. Rakić, A. D., Djurišić, A. B., Elazar, J. M. & Majewski, M. L. Optical properties of metallic films for vertical-cavity optoelectronic devices. *Appl. Opt.* **37**, 5271 (1998).

35. Shockley, W. & Queisser, H. J. Detailed balance limit of efficiency of p-n junction

solar cells. *J. Appl. Phys.* **32**, 510–519 (1961).

36. Nozik, A. J. Quantum Dot Solar Cells. *Phys. E* **14**, 115–120 (2002).

37. Lee, Y. K. *et al.* Hot carrier multiplication on graphene/TiO2 Schottky nanodiodes. *Sci. Rep.* **6**, 1–9 (2016).

38. Tielrooij, K. J. *et al.* Photoexcitation cascade and multiple hot-carrier generation in graphene. *Nat. Phys.* **9**, 248–252 (2013).

39. Song, J. C. W., Rudner, M. S., Marcus, C. M. & Levitov, L. S. Hot carrier transport and photocurrent response in graphene. *Nano Lett.* **11**, 4688–4692 (2011).

40. Groeber, M. A., Haley, B. K., Uchic, M. D., Dimiduk, D. M. & Ghosh, S. 3D reconstruction and characterization of polycrystalline microstructures using a FIB-SEM system. *Mater. Charact.* **57**, 259–273 (2006).

41. Okazumi, T., Ueda, K., Tajima, K., Umetsu, N. & Narushima, T. Anatase formation on titanium by two-step thermal oxidation. *J. Mater. Sci.* **46**, 2998–3005 (2011).

42. Aarik, J., Aidla, A., Mändar, H. & Uustare, T. Atomic layer deposition of titanium dioxide from TiCl4 and H2O: Investigation of growth mechanism. *Appl. Surf. Sci.* **172**, 148–158 (2001).

43. Scanlon, D. O. *et al.* Band alignment of rutile and anatase TiO2. *Nat. Mater.* **12**, 798–801 (2013).

44. Diamanti, M. V. & Pedeferri, M. P. Effect of anodic oxidation parameters on the titanium oxides formation. *Corros. Sci.* **49**, 939–948 (2007).

45. Diamanti, M. V., Codeluppi, S., Cordioli, A. & Pedeferri, M. P. Effect of thermal oxidation on titanium oxides' characteristics. *J. Exp. Nanosci.* **4**, 365–372 (2009).

46. Cronemeyer, D. C. Electrical and optical properties of rutile single crystals. *Phys. Rev.* **87**, 876–886 (1952).

47. Othman, M. A., Amat, N. F., Ahmad, B. H. & Rajan, J. Electrical Conductivity Characteristic of TiO2 Nanowires From Hydrothermal Method. *J. Phys. Conf. Ser.* **495**, 012027 (2014).

48. Rafizadeh, S. & Kangarlou, H. Study the Influence of Thermal Oxidation on the Structures of Titanium Very Thin Layers. *Proc. World Congr. Eng.* **II**, 6–8 (2011).

49. Yoshizawa, M., Kobayashi, M., Petrykin, V., Kato, H. & Kakihana, M. Insights into a selective synthesis of anatase, rutile, and brookite-type titanium dioxides by a hydrothermal treatment of titanium complexes. *J. Mater. Res.* **29**, 90–97 (2014).

50. Gemelli, E. & Camargo, N. H. a. Oxidation kinetics of commercially pure titanium. *Matéria (Rio Janeiro)* **12**, 525–531 (2007).

51. Kuromoto, N. K., Simão, R. A. & Soares, G. A. Titanium oxide films produced on commercially pure titanium by anodic oxidation with different voltages. *Mater. Charact.* **58**, 114–121 (2007).

52. Zhao, J., Wang, X., Chen, R. & Li, L. Fabrication of titanium oxide nanotube arrays by anodic oxidation. *Solid State Commun.* **134**, 705–710 (2005).

53. Macák, J. M., Tsuchiya, H. & Schmuki, P. High-aspect-ratio TiO2 nanotubes by anodization of titanium. *Angew. Chemie - Int. Ed.* **44**, 2100–2102 (2005).

54. Crawford, G. A., Chawla, N., Das, K., Bose, S. & Bandyopadhyay, A.

Microstructure and deformation behavior of biocompatible TiO2 nanotubes on titanium substrate. *Acta Biomater.* **3**, 359–367 (2007).

55. Vijayalakshmi, R. & Rajendran, V. Synthesis and characterization of nano-TiO2 via different methods. *Sch. Res. Libr.* **4**, 1183–1190 (2012).

56. Windt, D. L. *et al.* Optical constants for thin films of Ti, Zr, Nb, Mo, Ru, Rh, Pd, Ag, Hf, Ta, W, Re, Ir, Os, Pt, and Au from 24 Åto 1216 Å. *Appl. Opt.* **27**, 246–278 (1988).

57. Siefke, T. *et al.* Materials Pushing the Application Limits of Wire Grid Polarizers further into the Deep Ultraviolet Spectral Range. *Adv. Opt. Mater.* **4**, 1780–1786 (2016).

58. Ahmed, K. & Chiang, T. Schottky barrier height extraction from forward current-voltage characteristics of non-ideal diodes with high series resistance. *Appl. Phys. Lett.* **102**, (2013).

59. Rawat, G., Kumar, H., Kumar, Y., Kumar, C. & Somvanshi, D. Effective Richardson Constant of Sol-Gel Derived TiO2 Films in n-TiO2/p-Si Heterojunctions. *IEEE Electron Device Lett.* **38**, 633–636 (2017).

60. Bhatnagar, M., Baliga, B. J., Kirk, H. R. & Rozgonyi, A. Effect of Surface Inhomogeneities on the Electrical Characteristics of SiC Schottky Contacts. *IEEE Trans. Electron Devices* **43**, 150–156 (1996).

61. Fair, R. *Rapid Thermal Processing*. (Academic Press, 1993).

62. Baliga, B. J. *The IGBT Device*. (William Andrew Publishing, 2015).

63. Chung, C. K. & Liao, M. W. Study of phase transformation of rapid-thermal-

annealed TiO x films and their photo-induced hydrophilicity. *J. Am. Ceram. Soc.* **95**, 1123–1127 (2012).

64. Roy, S., Ghosh, S. P., Pradhan, D., Sahu, P. K. & Kar, J. P. Investigation of morphological and electrical properties of RTA-processed TiO2 for memristor application. *J. Sol-Gel Sci. Technol.* **96**, 702–717 (2020).

VITA

Eric M. Acosta attended Purdue University in August 2011 and received the degree of Bachelor of Science in Nuclear Engineering in August 2015. During his senior year, he worked as a research assistant in the Department of Nuclear Engineering studying the effects of high energy helium bombardment on tungsten for nuclear fusion applications.

He entered the University of Missouri-Columbia in September of 2015 as a Ph.D. student in the Nuclear Engineering Program. During the first two years (2015-2017), he worked as a research assistant working on the prototype design and testing of radiolytic electrochemical batteries. From 2017 to 2019, he worked for a DoD SBIR project with responsibilities including semiconductor fabrication, power characterization of nuclear batteries, 3D CAD design, and grant proposal writing. During his graduate career, he presented his work titled "Wave Nature of Beta Particles and their Interaction with Surface Plasmons" at the American Nuclear Society Winter 2018 meeting in Orlando, FL. He was first author on the publication titled "Effects of Beta Radiation on Schottky Barrier Height in Nanoporous TiO2" (under review at the time of this writing) and co-author on the publication titled " Properties of doped GaN through a neutron transmutation doping process with high epithermal neutron flux" (under review at the time of this writing). He received the degree of Doctor of Philosophy in Nuclear Engineering in December 2021.